The Astrophysical Journal, 974:58 (15pp), 2024 October 10 https://doi.org/10.3847/1538-4357/ad6b95

An Eddington-limited Accretion Disk Wind in the Narrow-line Seyfert 1 PG 1448+273

J. N. Reeves[1,2], V. Braito[1,2,3], A. Luminari[4,5], D. Porquet[6], M. Laurenti[7,8], G. Matzeu[9], A. Lobban[10], and S. Hagen[11]
[1] Department of Physics, Institute for Astrophysics and Computational Sciences, The Catholic University of America, Washington, DC 20064, USA; reevesjn@cua.edu
[2] INAF, Osservatorio Astronomico di Brera, Via Bianchi 46 I-23807 Merate (LC), Italy
[3] Dipartimento di Fisica, Università di Trento, Via Sommarive 14, Trento 38123, Italy
[4] INAF—IAPS, via del Fosso del Cavaliere 100, 00100 Roma, Italy
[5] INAF—Osservatorio Astronomico di Roma, Via Frascati 33, 00078 Monteporzio, Italy
[6] Aix-Marseille Univ., CNRS, CNES, LAM, Marseille, France
[7] Dipartimento di Fisica, Università di Roma "Tor Vergata," Via della Ricerca Scientifica 1, 00133 Roma, Italy
[8] Space Science Data Center, SSDC, ASI, Via del Politecnico snc, 00133 Roma, Italy
[9] Quasar Science Resources SL for ESA, European Space Astronomy Centre (ESAC), Science Operations Department, 28692, Villanueva de la Cañada, Madrid, Spain
[10] European Space Astronomy Centre (ESA/ESAC), E-28691 Villanueva de la Canada, Madrid, Spain
[11] Centre for Extragalactic Astronomy, Department of Physics, University of Durham, South Road, Durham, DH1 3LE, UK
Received 2024 March 11; revised 2024 July 21; accepted 2024 August 4; published 2024 October 4

Abstract

PG 1448+273 is a luminous, nearby ($z = 0.0645$), narrow-line Seyfert 1 galaxy, which likely accretes close to the Eddington limit. Previous X-ray observations of PG 1448+273 with XMM-Newton in 2017 and NuSTAR in 2022 revealed the presence of an ultrafast outflow, as seen through its blueshifted iron (Fe) K absorption profile, where the outflow velocity appeared to vary in the range $0.1-0.3c$. In this work, new X-ray observations of PG 1448 +273 are presented, in the form of four simultaneous XMM-Newton and NuSTAR observations performed in 2023 July and August. The X-ray spectra appeared at a similar flux in each observation, making it possible to analyze the mean 2023 X-ray spectrum at high signal-to-noise ratio. A broad ($\sigma = 1$ keV) and highly blueshifted ($E = 9.8 \pm 0.4$ keV) Fe K absorption profile is revealed in the mean spectrum. The profile can be modeled by a fast, geometrically thick accretion disk wind, which reveals a maximum terminal velocity of $v_\infty = -0.43 \pm 0.03c$, one of the fastest known winds in a nearby active galactic nucleus. As a result, the inferred mass outflow rate of the wind may reach a significant fraction of the Eddington accretion rate.

Unified Astronomy Thesaurus concepts: X-ray astronomy (1810); High-luminosity active galactic nuclei (2034)

1. Introduction

Since their initial discovery two decades ago (Chartas et al. 2002; Pounds et al. 2003; Reeves et al. 2003), ultrafast outflows (or UFOs) in X-rays have been found to occur in about 40% of active galactic nuclei (AGNs; Tombesi et al. 2010). Most of these detections arise through studies of the iron (Fe) K band toward nearby and X-ray-bright, local ($z < 0.1$) Seyfert 1 AGNs, with typical outflows velocities of around $0.1c$ (e.g., Tombesi et al. 2010; Gofford et al. 2013; Igo et al. 2020; Matzeu et al. 2023). The mechanical power of these winds can typically reach up to a few percent of the Eddington limit (Tombesi et al. 2013; Gofford et al. 2015), sufficient to provide significant mechanical feedback into the AGN host galaxy (Silk & Rees 1998; Fabian 1999; King 2003; Di Matteo et al. 2005; Hopkins & Elvis 2010). Powerful black hole winds may also play a crucial part in regulating the growth of supermassive black holes in more luminous quasars (Nardini et al. 2015; Tombesi et al. 2015; Matzeu et al. 2023) and notably at high redshifts near the peak of the QSO evolution (e.g., Chartas et al. 2021, and references therein).

At lower redshifts, the narrow-line Seyfert 1 s (NLS1s; Osterbrock & Pogge 1985) represent a part of the AGN population with relatively low black hole masses, yet with high accretion rates with respect to the Eddington limit (Boroson 2002). As such, they provide an excellent laboratory for studying accretion disk winds, which produce the observed UFOs (Proga & Kallman 2004; Sim et al. 2008; Fukumura et al. 2010; Sim et al. 2010; Mizumoto et al. 2021). Several notable examples of UFOs have been detected in nearby NLS1s (Pounds & Vaughan 2012; Longinotti et al. 2015; Hagino et al. 2016; Parker et al. 2017; Kosec et al. 2018; Reeves & Braito 2019), expanding the parameter space of AGN accretion disk winds into the high-accretion-rate regime.

The subject of this paper is the nearby ($z = 0.0645$) NLS1 PG1448+273, which also shows evidence for a powerful UFO, observed both in the Fe K band and at soft-X-ray energies (Kosec et al. 2020; Laurenti et al. 2021; Reeves et al. 2023). It is also classed as a radio-quiet QSO (Schmidt & Green 1983) and has narrow permitted lines, e.g., a Hβ FWHM of 1330 km s^{-1} (Grupe et al. 2004), with a bolometric luminosity estimated to be $L_{\rm bol} = 2-3 \times 10^{45}$ erg s^{-1} (e.g., Grupe et al. 2004; Rakshit et al. 2020). Recently, a black hole mass estimate of $M_{\rm BH} = 1.01^{+0.38}_{-0.23} \times 10^7\ M_\odot$ was derived by Hu et al. (2021), obtained from a Hβ-based reverberation study of 15 PG quasars. Given its observed bolometric luminosity, this implies that PG1448+273 is likely to accrete near the Eddington limit, which may provide favorable conditions for launching an accretion disk wind, as discussed by Giustini & Proga (2019).

The detection of a fast wind in PG1448+273 was initially obtained by Kosec et al. (2020) and Laurenti et al. (2021; see their Figures 3 and 1, respectively), on the basis of a 75 ks XMM-Newton exposure in 2017. This 2017 XMM-Newton observation occurred just prior to a pronounced dip as observed

by the Swift monitoring (Laurenti et al. 2021), resulting in an historically low X-ray flux for PG1448+273. An Fe K absorption trough was measured centered at 7.5 keV, which implied an outflow velocity of $\sim 0.1c$, assuming an identification with the $1s \rightarrow 2p$ resonance lines from He-like (Fe XXV) and H-like (Fe XXVI) iron. It has one of the deepest absorption profiles among the UFOs reported to date (see Tombesi et al. 2010; Gofford et al. 2013), with an equivalent width of $\mathrm{EW} = -410 \pm 80$ eV. As was inferred by Kosec et al. (2020) and Laurenti et al. (2021), the high equivalent width implies an absorption column density of the order $N_{\mathrm{H}} = 10^{24}$ cm^{-2}. In particular, the whole absorption profile studied by Laurenti et al. (2021) was modeled with a physically motivated accretion disk-wind model, utilizing the Wind in the Ionized Nuclear Environment (WINE) code of Luminari et al. (2018).

The first NuSTAR observation of PG1448+273 (250 ks duration, 125 ks exposure) occurred in 2022 January and revealed strong X-ray variability (Reeves et al. 2023). The first part of the observation (slice A), seen at a much higher flux ($F_{2-10} = 4.8 \times 10^{-12}$ erg cm^{-2} s^{-1}), was coincident with a 70 ks XMM exposure and the wind absorption at Fe K had diminished in opacity compared to 2017. During the last 60 ks with NuSTAR (slice B), a deep ($>2\times$) and rapid (<10 ks) drop in flux was observed and was also accompanied by an increase in spectral hardness. The slice B NuSTAR spectrum revealed a deep Fe K absorption trough at 9 keV and could be modeled by a disk-wind model (Sim et al. 2008, 2010; Matzeu et al. 2022) of terminal velocity $v_{\infty} = -0.26 \pm 0.03c$, which implies at least a factor of 2 increase in wind velocity compared to the original 2017 observation. Thus, the wind in PG1448+273 appears to be strongly variable, both in its opacity and velocity, reminiscent of the drastic velocity changes in MCG–3–58–07 ($v/c \sim 0.07 \rightarrow 0.2$; Braito et al. 2022).

This paper presents a follow-up of the Reeves et al. (2023) work, where subsequently four new simultaneous XMM-Newton and NuSTAR observations of PG1448+273 were performed in 2023 July and August. The observations were also coordinated with daily Swift monitoring, to measure the overall variability of PG1448+273 throughout the campaign. In these new observations, the Fe K wind profile is found to be both velocity broadened and blueshifted up to 10 keV in the X-ray spectra, revealing one of the fastest known UFOs in an AGN X-ray spectrum. The overall profile can be modeled by a geometrically thick disk wind, which achieves a maximum terminal velocity of $v_{\infty} = -0.43 \pm 0.03c$. The subsequent mass outflow rate is inferred to be close to the Eddington rate in this high-accretion-rate AGN.

The paper is organized as follows. In Section 2, the observations and data reduction are described, while in Section 3 the AGN variability is quantified through the XMM-Newton, NuSTAR, and Swift observations. Section 4 presents the results of the physically motivated disk-wind modeling, where the velocity range and mass outflow rate of the AGN wind are inferred. Section 5 quantifies any wind variability within the 2023 campaign and is compared with past observations. Section 6 then compares the properties of the wind in PG1448+273 with other AGNs, while the wind energetics and plausible launching mechanisms are discussed. Throughout the paper, 90% confidence intervals for one parameter of interest are adopted for the uncertainties (or $\Delta\chi^2 = 2.7$), while parameters are stated in the AGN rest frame at $z = 0.0645$. The standard Lambda cold dark matter (ΛCDM) cosmology ($H_0 = 70$ km s^{-1} Mpc^{-1}, $\Omega_m = 0.3$, $\Omega_{\Lambda} = 0.7$) is adopted throughout the paper.

2. Observations and Data Reduction

The 2023 X-ray campaign of PG1448 + 273 encompassed four observations with XMM-Newton (Jansen et al. 2001) and NuSTAR (Harrison et al. 2013) in 2023 July–August, with a spacing of about 2 weeks between each observation; see Table 1 for the observation log of the campaign. The Swift campaign consisted of 39 daily X-Ray Telescope (XRT; Burrows et al. 2005) snapshots of approximate 1 ks duration from 2023 June to August, in order to provide temporal coverage over the entire XMM-Newton and NuSTAR campaign. The Swift/XRT data were processed with v0.13.7 of the XRTPIPELINE to create the lightcurves and spectra. A circular source extraction region of 20″ was used, while for the background an annulus of radii 40″ and 130″ centered on the source was adopted.

The first and third of the XMM-Newton observations (hereafter OBS 1 and OBS 3) covered a duration of about a day (86.1 ks and 73.2 ks, respectively), as measured from the start and stop times of the sequences (see Table 1). The second XMM-Newton observation (OBS 2) was interrupted by a strong solar flare of 5 hr duration, and the telescope filter wheel was subsequently closed during this time (CAL CLOSED position). As a result, the second XMM-Newton observation was split into two separate sequences either side of the solar flare (hereafter OBS 2a and 2b), of duration 11.8 ks and 45.9 ks, respectively. The fourth XMM-Newton observation (OBS 4) was scheduled as a result of the exposure time lost during the second observation and was of shorter (22.1 ks) duration. Each of the XMM-Newton observations were performed simultaneously with NuSTAR at hard-X-ray energies. All four NuSTAR observations covered a total duration of about 100 ks each, in order to overlap with the start and stop times of each of the XMM-Newton exposures, while the fourth XMM-Newton observation coincided with the start of the corresponding NuSTAR exposure (see Table 1). The XMM-Newton EPIC-pn (Strüder et al. 2001) exposures were performed in Large Window mode, with the medium filter applied, while the EPIC-MOS (Turner et al. 2001) exposures were in Small Window mode.

The XMM-Newton and NuSTAR observations were processed using the NUSTARDAS v2.1.2, XMM-Newton SAS v20.0, and HEASOFT v6.30 software. Background screening was performed on the XMM-Newton observations, in order to remove periods of high background due to solar flares during the course of each XMM-Newton orbit. A background cut of >1 cts s^{-1} from 10 to 12 keV over the entire EPIC-pn field of view was applied to select Good Time Intervals of low background for subsequent spectral extraction. While the first and fourth observations were free of background flares, a strong solar flare affected XMM-Newton OBS 2 (as noted above). As a result, the net EPIC-pn exposures were reduced to 6.3 and 34.3 ks for the OBS 2a and OBS 2b sequences, respectively. A portion of XMM-Newton OBS 3 was also affected by background flares, which resulted in a reduction of the net exposure to 53.4 ks for spectral extraction. The NuSTAR exposures were screened for passage through the South Atlantic Anomaly (SAA), resulting in net exposures of between 51 and 54 ks per focal plane module (FPM) per observation; this is typical of the 50% observing efficiency in a

Table 1
Observation Log for the 2023 XMM-Newton, NuSTAR, and Swift Campaigns of PG1448+273

Observation	Sequence	Start Time (UT)	End Time (UT)	Duration (ks)	Net Exp (ks)[a]	Rate (s^{-1})[b]	Flux[c]
NuSTAR 1	6092001002	2023/07/05 22:16:09	2023/07/07 03:06:09	103.8	51.7	0.074 ± 0.002	3.2
NuSTAR 2	6092001004	2023/07/17 18:36:09	2023/07/19 00:56:09	109.2	51.1	0.069 ± 0.002	3.0
NuSTAR 3	6092001006	2023/08/02 16:51:09	2023/08/03 23:06:09	108.9	52.4	0.062 ± 0.002	2.7
NuSTAR 4	6092001008	2023/08/17 10:11:09	2023/08/18 15:01:09	103.8	54.2	0.063 ± 0.002	2.8
NuSTAR mean					196.1[d]	0.069 ± 0.001	3.0
XMM-Newton 1	0920250201	2023/07/06 00:58:34	2023/07/07 00:53:57	86.1	80.3	3.555 ± 0.007	5.9
XMM-Newton 2a	0920250301	2023/07/18 00:09:33	2023/07/18 03:25:52	11.8	6.3	2.108 ± 0.022	3.7
XMM-Newton 2b	0920250301	2023/07/18 08:33:29	2023/07/18 21:18:44	45.9	34.3	3.646 ± 0.010	5.9
XMM-Newton 3	0920250401	2023/08/02 18:11:32	2023/08/03 16:31:34	73.2	53.4	3.216 ± 0.008	5.1
XMM-Newton 4	0920250601	2023/08/17 09:55:40	2023/08/17 16:04:02	22.1	20.6	3.842 ± 0.014	6.1
XMM-Newton mean					188.6[d]	3.481 ± 0.004	5.8
Swift/XRT (OBS 1–39)[e]	00097192	2023/06/25 10:12:35	2023/08/14 11:08:56		35.5 (total)	0.071 ± 0.008	2.0 (low)
						0.389 ± 0.028	12.3 (high)
						0.181 ± 0.013	5.3 (mean)

Notes.
[a] Net exposure, for XMM-Newton (EPIC-pn), NuSTAR, and Swift/XRT, correcting for background screening, SAA passage, and detector deadtime.
[b] Net count rates per XMM-Newton (EPIC-pn), Swift/XRT, or NuSTAR observation.
[c] Observed flux measured from 0.5 to 10 keV for XMM-Newton (EPIC-pn) and Swift/XRT and 3–30 keV band for NuSTAR. Units are $\times 10^{-12}$ erg cm^{-2} s^{-1}.
[d] The total exposure time of the mean spectrum excludes the short lower-flux OBS 2a XMM-Newton sequence and the corresponding dip portion of the second NuSTAR observation, from 20 to 50 ks as measured from the start of that observation (see Figure 2).
[e] The minimum, maximum, and mean count rates and fluxes are given across all 39 SwiftXRT observations.

low Earth orbit. Table 1 summarizes all of the resulting exposures.

NuSTAR source spectra were extracted using a 45″ circular region centered on the source and two background circular regions with a 45″ radius and clear from stray light. XMM-Newton EPIC-pn spectra were extracted from single and double events (patterns 0–4), using a 35″ source region and 2″ × 35″ background regions on the same chip. EPIC-MOS spectra were extracted using patterns 0–12, using a 30″ source region and 2″ × 36″ background regions. The effective area of the EPIC CCD detectors was corrected at high energies through the SAS task ARFGEN by applying the option APPLYABSFLUXCORR.[12] This option provides an improved cross-calibration for simultaneous observations between NuSTAR and XMM-Newton over the overlapping 3–10 keV range. For each observation, the spectra and responses from the individual FPMA and FPMB detectors on board NuSTAR were combined into a single spectrum after they were first checked for consistency. The NuSTAR spectra were utilized over the 3–30 keV band; above 30 keV, the source spectrum becomes background dominated as the source count rate declines. The total NuSTAR background count rate over this band is approximately 6% of the source rate. For EPIC-pn, the background rate after filtering is about 4% over the 3–10 keV band and negligible at soft X-rays.

As the effective area of the EPIC-pn detector is about a factor of 8 larger than that of each EPIC-MOS CCD at 9 keV, where the high-energy absorption feature in PG1448+273 occurs (see Section 4), we used only the EPIC-pn and NuSTAR data in the detailed spectral analysis. Nonetheless, the MOS spectra are found to be consistent with the EPIC-pn across the 0.3–10 keV band. All the spectra are binned to a minimum of 100 counts per bin to ensure a minimum signal-to-noise ratio (S/N) of 10 in the spectra and χ^2 minimization was used for the subsequent spectral fitting. Count rates and fluxes for each of the exposures are listed in Table 1.

Spectra from the XMM-Newton Reflection Grating Spectrometer (RGS; den Herder et al. 2001) for all of the 2023 observations were extracted using the RGSPROC pipeline. These were combined into a single RGS 1+2 spectrum for each observation using using RGSCOMBINE, after first checking that the individual RGS 1 and RGS 2 spectra were consistent with each other within the errors. Furthermore, very little variability was observed over the four epochs (OBS 1, 2b, 3, and 4) in the RGS band; the 0.4–2.0 keV flux ranged between 3.6 and 4.1 $\times 10^{-12}$ erg cm^{-2} s^{-1}, while no spectral variations were seen. As a result, all of these epochs were combined into a single 2023 RGS spectrum to maximize S/N, with the exception of the very short OBS 2a sequence, which has very low S/N. The total net count rate obtained over the 6–30 Å band (RGS 1+2 combined) was 0.195 ± 0.001 cts s^{-1}, with a net exposure of 141.7 ks. The spectra were binned in constant wavelength bins of $\Delta\lambda = 0.1$ Å, which approximates the spectral resolution of the RGS gratings.

3. Overall AGN Variability

Figure 1 shows the fluxed Swift/XRT lightcurve of PG1448+273 during the 2023 campaign. Here, the AGN displayed a factor of 6 variability, covering a range of 0.5–10 keV flux from 2 to 12 $\times 10^{-12}$ erg cm^{-2} s^{-1}. Several mini X-ray flares are apparent in the lightcurve, the most notable occurring at the end of the Swift monitoring. For comparison, the mean fluxes of each of the XMM-Newton observations are overlaid on the Figure 1 lightcurve as blue squares. In contrast to the variability amplitude caught by Swift, each of the XMM-Newton observations (OBS 1, 2b, 3, and 4) caught the source at a very similar flux, covering a narrow range from $F_{0.5-10\,\mathrm{keV}} = 5.1-6.1 \times 10^{-12}$ erg cm^{-2} s^{-1} and close to the mean Swift flux

[12] https://xmmweb.esac.esa.int/docs/documents/CAL-SRN-0388-1-4.pdf

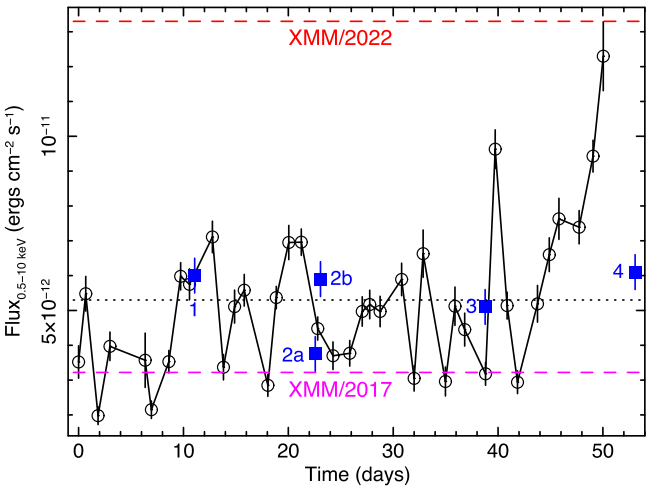

Figure 1. Swift/XRT lightcurve of PG1448+273 from the 2023 monitoring campaign, where time is measured in days from the start time of the Swift monitoring listed in Table 1. The 0.5–10 keV XRT lightcurve (black circles) exhibits a factor of 6 variability over the whole campaign. In comparison, the 0.5–10 keV flux measured from the four XMM-Newton observations (blue squares) shows little variability between each sequence, with the exception of the short OBS 2a sequence. Overall, the XMM-Newton observations captured the source close to the average Swift flux in the campaign, as is shown by the black dotted horizontal line. In contrast, two previous XMM-Newton observations of PG1448+273 in 2017 and 2022 spanned the range of Swift flux, as is indicated by the magenta and red horizontal dashed lines. Thus, the 2023 XMM-Newton observations resemble an average flux state of PG1448+273.

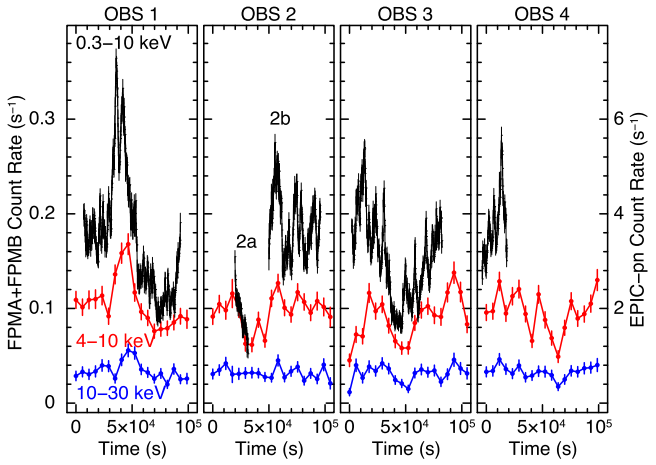

Figure 2. Background-subtracted lightcurves from the 2023 XMM-Newton and NuSTAR observations of PG1448+273. The *x*-axis shows the time elapsed for each observation, compared to the start time of each NuSTAR exposure, while the *y*-axis shows the count rates for NuSTAR (FPMA+FPMB) and EPIC-pn (right-hand axis). The 0.3–10 keV EPIC-pn lightcurve is shown in black in 200 s bins, while NuSTAR is shown in red and blue, over the 4–10 keV and 10–30 keV bands, respectively, and are binned into 5814 s orbital bins. Note the gap in XMM-Newton OBS 2, split into two sequences (2a and 2b as marked), was due to the solar flare which interrupted the observation. Overall, the average source flux was similar between each of the observations, while a notable flare was observed in OBS 1 and OBS 2a appears to coincide with a short dip in the lightcurve. The variability amplitude in the hardest 10–30 keV band is modest in comparison.

of $F_{0.5-10\,\mathrm{keV}} = 5.3 \times 10^{-12}$ erg cm^{-2} s^{-1}. The only exception to this occurs at the very start of the second XMM-Newton observation (OBS 2a sequence), where the AGN was seen at a lower flux of $F_{0.5-10\,\mathrm{keV}} = 3.7 \times 10^{-12}$ erg cm^{-2} s^{-1}. Even the fourth XMM-Newton observation caught the AGN close to the average Swift flux, despite it occurring a few days after the strong X-ray flare at the end of the Swift lightcurve. The lack of any strong variability comparing each of the 2023 XMM-Newton observations also contrasts with two recent XMM-Newton observations of PG1448+273, in 2017 and 2022, which encompass the range of fluxes observed in the Swift lightcurve; see Figure 1. In contrast, the four 2023 XMM-Newton observations appear to probe an average flux state of this AGN.

X-ray lightcurves were also extracted for each of the observations over the full 0.3–10 keV band for EPIC-pn, using time bins of 200 s and over the 4–10 keV and 10–30 keV bands for NuSTAR, using orbital bins of 5814 s duration; these are plotted in Figure 2. As can be seen from the lightcurves, the mean fluxes across all of the observations are similar, while a factor of 2 variability on shorter kiloseconds timescales is observed. In particular, a strong flare is observed in OBS 1, which is apparent across both the XMM-Newton and NuSTAR lightcurves, while the start of OBS 2a coincides with a factor of 2 dip in flux. Unfortunately, the recovery from this dip is missed by XMM-Newton as it occurs during the CAL CLOSED segment of OBS 2, although the 4–10 keV band NuSTAR lightcurve does capture the dip from 20 to 50 ks in its entirety. The highest-energy band (10–30 keV) exhibits little variability, indicating the intrinsic hard-X-ray continuum remained relatively steady over the entire campaign.

4. X-Ray Spectral Analysis

A simple comparison of the individual spectra was then performed across all four of the XMM-Newton observations,

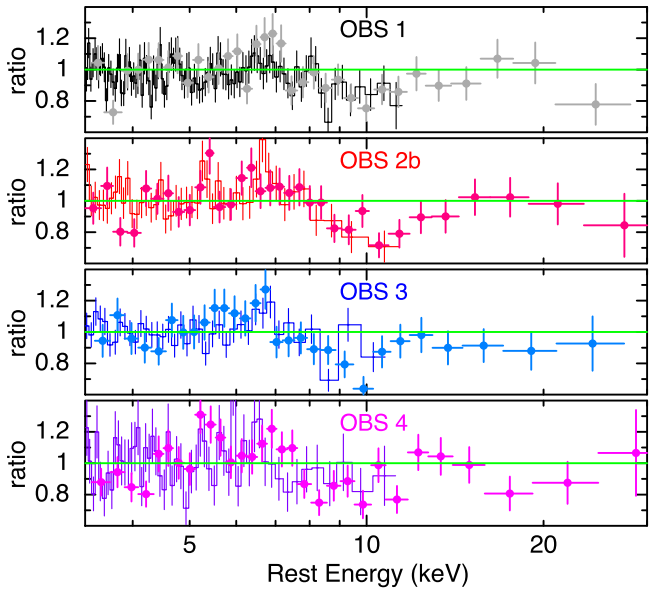

Figure 3. The four panels show the simultaneous XMM-Newton and NuSTAR (filled circles) spectra for OBS 1, 2b, 3, and 4 (top to bottom), plotted as a ratio to a power law over the 3–30 keV band. Note the deficit of counts observed from 8 to 12 keV in each case, highlighting the presence of an absorption trough.

excluding the very short OBS 2a dip exposure. The XMM-Newton spectra were fitted with a simple power-law model modified by Galactic absorption, along with their corresponding simultaneous NuSTAR spectra over the 3–30 keV band. Figure 3 shows the spectra plotted as a data-to-model ratio to the above power-law model. None of the spectra show a significant variation in photon index within $\Delta\Gamma = 0.1$ (e.g., OBS 1, $\Gamma = 2.17 \pm 0.03$, versus OBS 4, $\Gamma = 2.23 \pm 0.05$). The

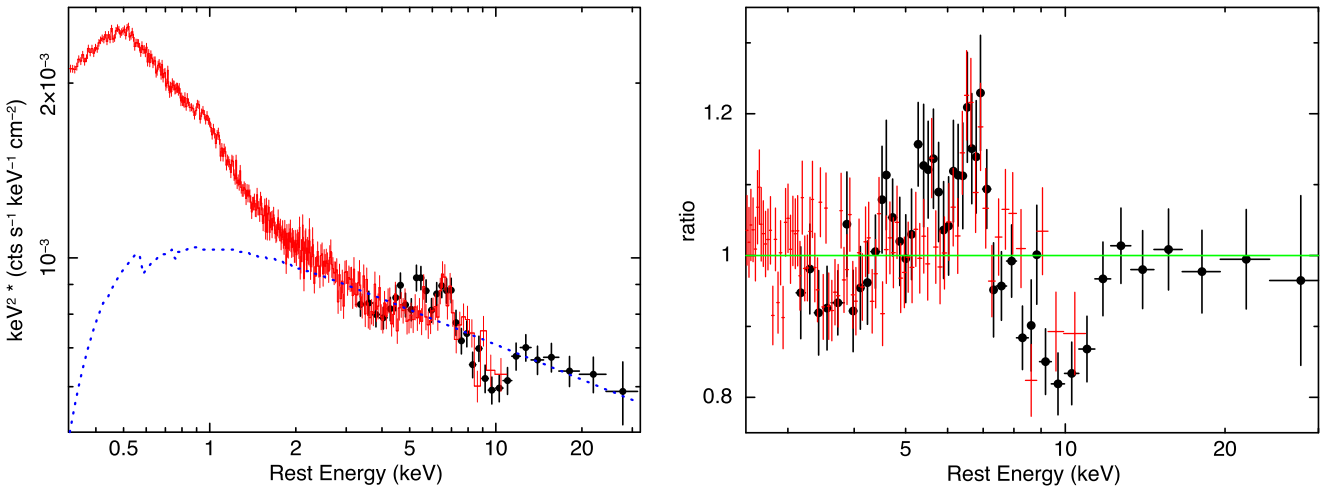

Figure 4. Mean XMM-Newton EPIC-pn and NuSTAR X-ray spectra of PG1448+273. The pn is shown in red and NuSTAR FPMA+B as black circles. The left panel shows the fluxed spectrum, where the count rate spectrum has been divided by the instrumental effective area and multiplied twice by energy and thus the flux is in νF_ν units. The dotted blue line shows the approximate level of the hard-X-ray power-law continuum, modified by Galactic absorption. The strong soft-X-ray excess is apparent above the power law. Note the cross-normalization factor of 1.14 between NuSTAR and XMM-Newton is accounted for in the plot. The right panel shows the data-to-model ratio to the baseline two-component continuum model described in Section 4. Both plots highlight the strong absorption trough centered near 10 keV in the AGN rest frame, while Fe K-band emission is observed between 5 and 7 keV.

hard-X-ray flux, as measured by NuSTAR, also shows little variation ($F_{3-30\,\mathrm{keV}} = 2.7-3.1 \times 10^{-12}$ erg cm^{-2} s^{-1}). Negative residuals are also present in each of the ratio spectra between 8 and 12 keV, indicating the presence of Fe K absorption, and positive residuals are observed between 5 and 7 keV, indicating emission. Below 3 keV, all of the spectra show a smooth soft-X-ray excess above the power-law continuum, with very similar fluxes over the four observations (Table 1).

The individual 3–30 keV band spectra were fitted by adding a broadened Gaussian absorption profile to the power-law continuum to model the absorption trough between 8 and 12 keV. This is well modeled at a rest-frame energy of $E = 9.8 \pm 0.4$ keV, with a width of $\sigma = 1.2 \pm 0.5$ keV; this improved the fit statistic from $\chi^2/\nu = 200.4/131$ (power-law only) to $\chi^2/\nu = 147.2/125$ (with absorption profile). The absorption-line equivalent width does not vary across the four 2023 epochs, ranging from EW $= -465 \pm 180$ eV (OBS 1) to EW $= -570 \pm 210$ eV (OBS 4), i.e., the values are consistent within the errors. Likewise, allowing the line energy to vary between observations did not improve the fit ($\Delta\chi^2 < 2$), where the energy varies by <0.5 keV. Thus, the Fe K absorption profile does not appear to vary between observations.

Thus, given the lack of spectral variability across the 2023 observations, a mean spectrum was created for both the EPIC-pn and NuSTAR data, in order for the Fe K region to be characterized at high S/N. The mean spectra include all time intervals, except for the short OBS 2a XMM-Newton sequence and the corresponding dip period between 20 and 50 ks as seen in NuSTAR OBS 2 (13.3 ks net exposure). The net exposures of the mean spectra (after background screening) along with their count rates and fluxes are reported in Table 1. The spectra are also plotted in Figure 4 (left panel), which shows the mean fluxed spectra in νF_ν space, after multiplying twice by photon energy and being folded through the instrumental responses. The XMM-Newton and NuSTAR spectra are in good agreement, allowing for a small cross-normalization multiplicative factor between NuSTAR and EPIC-pn of $C = 1.14 \pm 0.02$. Note that the background level lies well below the source spectra (by more than an order of magnitude), except for the highest-energy NuSTAR bin at 30 keV. The spectra clearly reveal the structure in the Fe K region against the steep continuum, with an excess of counts peaking below 6–7 keV and a broad deficit between 8 and 12 keV, due to an absorption trough. The overall profile resembles the P Cygni–like wind profile observed in PDS 456 (Nardini et al. 2015).

A baseline model (model (a)) was constructed to fit the X-ray continuum between 0.3 and 30 keV. This consisted of two continuum components: a steep ($\Gamma > 2$) power law to account for the hard-X-ray emission, and a Comptonized disk component (the COMPTT model within XSPEC; Titarchuk 1994) for the soft-X-ray excess. Both of these are modified by the Galactic absorption column of $N_\mathrm{H} = 3 \times 10^{20}$ cm^{-2} (Kalberla et al. 2005) as modeled by the TBABS model (Wilms et al. 2000). The best-fit continuum parameters are reported in Table 2 (model (a)). In addition to the continuum form, a weak soft-X-ray emission line is required in the pn spectrum, at an energy of $E = 0.96 \pm 0.02$ keV and an equivalent width of EW $= 5.8 \pm 1.3$ eV. The emission-line width is unresolved at the pn resolution, with $\sigma < 0.07$ keV. Its possible origin has been discussed previously in Reeves et al. (2023) from the analysis of the 2022 RGS spectrum, and it likely arises from photoionized emission over the Ne band from larger-scale gas.

Although the baseline model provides a good description of the soft-X-ray band, the overall fit statistic is quite poor, with a reduced chi-squared of $\chi^2/\nu = 764/622$. Strong residuals arise over the 3–30 keV band, in the form of a broad Fe K emission and absorption profile (see Figure 4, right panel). Indeed, restricting the fit to just the 3–30 keV band yields a reduced chi-squared of $\chi^2/\nu = 315.5/194$, rejected with a null hypothesis probability of 8×10^{-8}.

To provide an initial nonphysical parameterization of the Fe K profile, both a Gaussian emission and absorption line were added to the baseline model. This returned a significant improvement in the fit statistic, to $\chi^2/\nu = 643.7/616$, while the fit statistic is also acceptable over the 3–30 keV band ($\chi^2/\nu = 193.7/188$). A broadened emission line was required, at a centroid energy of $E = 6.61 \pm 0.09$ keV, with an equivalent width

Table 2
Results of Spectral Fitting to Mean 2023 Spectrum

Parameter	Value
(a) Baseline Continuum:	
Photon index, Γ	2.20 ± 0.03
Power-law normalization ($N_{\rm PL}$)[a]	1.11 ± 0.04
Cross-normalization (NuSTAR/EPIC-pn)	1.14 ± 0.02
Seed photon temperature, T_0 (keV)	0.074 ± 0.004
Comptonization temperature, kT (keV)	$0.40^{+0.17}_{-0.09}$
Optical depth (τ)	$8.3^{+1.9}_{-2.0}$
Soft-X-ray flux ($F_{0.3-2\ \rm keV}$)[b]	5.4 ± 0.1
Fit statistic (baseline only), χ^2/ν	764.0/622
(b) Single Thin Disk Wind (Zone 1):	
Mass outflow rate ($\dot{M}_{\rm out}/\dot{M}_{\rm Edd}$)	0.67 ± 0.10
Ionizing luminosity (% $L_{2-10\ \rm keV}/L_{\rm Edd}$)	$1.4^{+0.3}_{-0.2}$
Terminal velocity parameter ($f_{\rm v}$)	$1.56^{+0.06}_{-0.17}$
Maximum terminal velocity ($v_{\rm max,\infty}/c$)	-0.39 ± 0.03
Inclination ($\mu = \cos\theta$)	0.64 ± 0.02
Fit satistic (single thin wind), χ^2/ν	685.8/618
(c) Additional Thin Disk Wind (Zones 2):	
Mass outflow rate ($\dot{M}_{\rm out}/\dot{M}_{\rm Edd}$)	0.48 ± 0.09
Ionizing luminosity (% $L_{2-10\ \rm keV}/L_{\rm Edd}$)	1.4[d]
Terminal velocity parameter ($f_{\rm v}$)	$0.93^{+0.16}_{-0.06}$
Maximum terminal velocity ($v_{\rm max,\infty}/c$)	-0.23 ± 0.03
Inclination ($\mu = \cos\theta$)	0.64[t]
Fit statistic (second thin wind), χ^2/ν	660.8/616
(d) Single Thick Disk Wind:	
Mass outflow rate ($\dot{M}_{\rm out}/\dot{M}_{\rm Edd}$)	$0.84^{+0.11}_{-0.12}$
Ionizing luminosity (% $L_{2-10\ \rm keV}/L_{\rm Edd}$)	0.80 ± 0.08
Terminal velocity parameter ($f_{\rm v}$)	1.72 ± 0.12
Maximum terminal velocity ($v_{\rm max,\infty}/c$)	-0.43 ± 0.03
Minimum terminal velocity ($v_{\rm min,\infty}/c$)	-0.25 ± 0.02
Inclination ($\mu = \cos\theta$)	0.58 ± 0.03
2–10 keV luminosity, ($L_{2-10\ \rm keV}$)[c]	2.6 ± 0.2
Fit statistic (single thick wind), χ^2/ν	646.3/618

Notes.
[a] Power-law normalization, in units of $\times\ 10^{-3}$ photons cm^{-2} s^{-1} keV^{-1} at 1 keV.
[b] Observed 0.3–2 keV flux, in units of $\times\ 10^{-12}$ erg cm^{-2} s^{-1}.
[c] Intrinsic 2–10 keV luminosity, corrected for wind absorption, in units of $\times\ 10^{43}$ erg s^{-1}.
[d] Denotes parameter is tied within the model.

of EW $= 143 \pm 26$ eV and a line width of $\sigma = 0.30^{+0.16}_{-0.10}$ keV. Interestingly, a very high centroid energy is found for the absorption profile, with $E = 9.8 \pm 0.4$ keV, which is significantly broadened ($\sigma = 1.1^{+0.5}_{-0.4}$ keV) and has a high equivalent width (EW $= -435^{+150}_{-190}$ eV). The parameters are also consistent with those obtained in the individual 2023 sequences. The centroid energy implies a blueshift of either $v/c \sim -0.33$ or $v/c \sim -0.36$ for an association with either H-like (at 6.97 keV) or He-like iron (at 6.7 keV), respectively. The degree of blueshift may be among the most extreme of those measured in nearby UFOs to date (Tombesi et al. 2010; Gofford et al. 2013; Igo et al. 2020; Luminari et al. 2021; Matzeu et al. 2023) and is at the highest end of the velocity range inferred for PDS 456 (Matzeu et al. 2017).

For a more physical parameterization of the absorber, the broad Gaussian absorption line was replaced by an XSTAR absorption model (Kallman et al. 2004), using the same

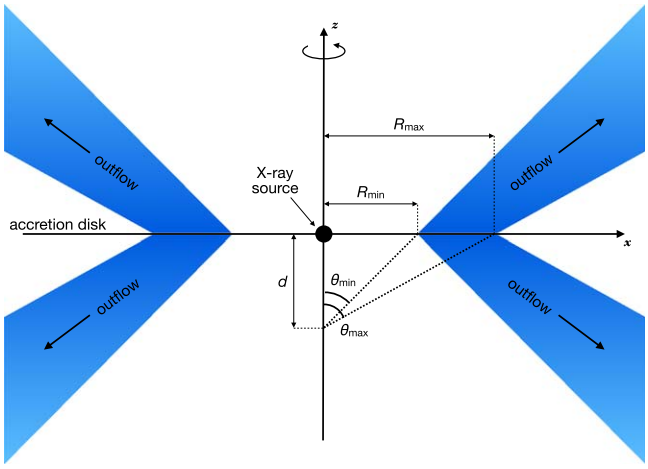

Figure 5. Schematic of the disk-wind geometry, adapted from Matzeu et al. (2022). The polar (z) and accretion disk axis (x) are shown as solid lines. The inner launching radius on the disk is $R_{\rm min}$ and the outer launching radius is $R_{\rm max}$. In the disk-wind models adopted here, the minimum launch radius is set to $32R_{\rm g}$ (in units of the gravitational radius). The outer launching radius is $R_{\rm max} = 48R_{\rm g}$ for the DW thin grid, while for the DW thick case $R_{\rm max} = 96R_{\rm g}$. Thus, the latter scenario corresponds to a geometrically thicker wind. The minimum opening angle of the wind streamline is $\theta_{\rm min}$ and is given by $\arctan(R_{\rm min}/d)$. In the models explored here, $R_{\rm min}/d = 1$ and thus $\theta_{\rm min} = 45°$. See Matzeu et al. (2022) and Sim et al. (2008, 2010) for a more detailed model description.

absorption grids used in the Reeves et al. (2023) paper on the 2022 data sets. A large turbulence velocity is used, with $v_{\rm turb} = 25{,}000$ km s^{-1}, to parameterize the breadth of the profile. The best-fit parameters of the XSTAR model are $N_{\rm H} = 6.2^{+1.3}_{-2.1} \times 10^{23}$ cm^{-2}, $\log\xi = 5.27^{+0.19}_{-0.13}$, and outflow velocity $v/c = -0.34 \pm 0.02$. Note the outflow velocity here corresponds to the point of maximum opacity in the profile, with an effective dispersion on the red and blue wings of $\pm 0.08c$ according to the turbulence velocity. The fit is statistically equivalent to the Gaussian case, with $\chi^2/\nu = 649.9/616$, while the inferred velocity is also consistent. The parameters are in broad agreement with those obtained by Reeves et al. (2023) for the lower-flux slice B interval of the 2022 NuSTAR observation.

Note in comparison to the broad ionized emission and absorption profile, only an upper limit can be placed on any narrow 6.4 keV Fe Kα fluorescence line, with an equivalent width of <30 eV. This is consistent with the X-ray Baldwin effect in higher-luminosity or higher-accretion-rate AGNs (Iwasawa & Taniguchi 1993; Bianchi et al. 2007)

4.1. Disk-wind Modeling

In order to model the Fe K wind signatures in the PG1448+273 spectra in a physical context, we utilized the radiative transfer disk-wind code developed by Sim et al. (2008, 2010, 2010). The disk-wind model provides a self-consistent treatment of both the emission and absorption arising from a biconical wind, as well as computing the (nonuniform) ionization structure and velocity field through the flow. Photoionization and atomic data are adopted from XSTAR (Kallman et al. 2004). The wind geometry is illustrated in Figure 5; see Matzeu et al. (2022) for a more detailed description.

This model has been previously employed to fit the Fe K wind absorption profiles in several AGNs, e.g., Mrk 766

(Sim et al. 2008), PG1211+143 (Sim et al. 2010), PDS 456 (Reeves et al. 2014), I Zw 1 (Reeves & Braito 2019), MCG −03−58−007 (Braito et al. 2022), PG1126−041 (Giustini et al. 2023), and most recently to the previous X-ray spectra of PG1448+273 (Reeves et al. 2023). Matzeu et al. (2022) expanded the parameter ranges covered by this wind model and tested the resulting grids on the prototype example of a fast disk wind in PDS 456. The FAST32 grid calculated by Matzeu et al. (2022) for this purpose was also recently applied to the previous (2017 and 2022) X-ray spectra of PG1448+273 (Reeves et al. 2023). Here, we test two variants of the `fast32` disk-wind model:

1. A *geometrically thin* accretion disk wind (hereafter DW thin), which is identical to the `fast32` grid calculated by Matzeu et al. (2022). Here, the inner launch radius is $R_{\rm min} = 32R_{\rm g}$ (in gravitational units), while the outer launch radius on the disk surface is $R_{\rm max} = 48R_{\rm g}$.
2. A *geometrically thick* accretion disk wind (hereafter DW thick), where the inner launch radius is $R_{\rm min} = 32R_{\rm g}$ and the outer launch radius is increased to $R_{\rm max} = 96R_{\rm g}$.

For clarity, we give the velocities and terminal velocities attained in the wind, as originally defined in Sim et al. (2008, 2010). Consider the velocity as a function of distance along the flow launched at a single point off the disk. This is expressed in a simple analytical form, where the velocity along the flow (v_l) increases versus the length along the flow (l). This is parameterized in Sim et al. (2008), as per their Equation (1), where

$$v_l = v_0 + (v_\infty v_0)\left(1 - \frac{R_v}{R_v + l}\right)^\beta. \quad (1)$$

Here, v_0 is the initial velocity at launch, while $R_{\rm v}$ is the radius at which the acceleration starts to occur. In the models adopted here, computed in Matzeu et al. (2022, see their Table 1), $R_v = R_{\rm min}$, i.e., the wind accelerates from the launch point, $v_0 = 0$ (the initial outwards velocity is deemed negligible), and $\beta = 1$ (the velocity power-law index). Thus, with increasing length (l) along the flow, the velocity quickly tends to the terminal velocity, v_∞.

Furthermore, the wind will not just be launched at a single specific radius, but over multiple radii on the disk, producing a range of terminal velocities originating at different launch radii (between $R_{\rm min}$ and $R_{\rm max}$). The terminal velocities realized in the wind models are determined via the launch radius and the terminal velocity parameter ($f_{\rm v}$), where

$$v_\infty/c = f_{\rm v}\sqrt{2/R}, \quad (2)$$

where R is the launch radius in gravitational units. In the spectral fitting, the terminal velocity is adjusted by varying the $f_{\rm v}$ parameter, where $f_{\rm v}$ physically corresponds to the scaling factor between the escape velocity at a radius R on the disk and the final terminal velocity. The effect of gravity upon the terminal velocity is also accounted for in the disk-wind model, by extrapolation back to the launch point of a wind streamline. Thus, for $f_v = 1$, the wind is launched reaching exactly the escape velocity from the system.

The range in terminal velocities produced by the wind is thus governed by the range in launch radii as well as the $f_{\rm v}$ parameter. For example, in the case of $f_{\rm v} = 1.5$, then from Equation (2), the terminal velocities attained in the DW thick grid range from $v_\infty/c = 0.21$ to 0.375, where the fastest velocity is launched at the innermost launch radius of $R_{\rm min} = 32R_{\rm g}$ and the slowest (outermost radius) at $R_{\rm max} = 96R_{\rm g}$. In contrast, the DW thin grid covers a much smaller range of terminal velocities over the narrower range of launch radii from $R_{\rm min} = 32R_{\rm g}$ to $R_{\rm max} = 48R_{\rm g}$, e.g., for $f_{\rm v} = 1.5$, then $v_\infty/c = 0.31-0.375$. Thus, the thicker the streamline is in terms of $R_{\rm max}/R_{\rm min}$, the greater the range of velocities realized by the wind. As a result, the DW thick grid will tend to produce broader absorption profiles due to a larger velocity shear, as the sightline through the wind can intercept a wider range of terminal velocities compared to the DW thin case. The free parameters in the model are then as follows:

1. The terminal velocity parameter, $f_{\rm v}$, which covers the range from $f_{\rm v} = 0.25$ to 2.0 and determines the range of terminal velocities computed.
2. The inclination angle, $\mu = \cos\theta$, where θ is measured with respect to the polar axis and the minimum wind opening angle ($\theta_{\rm min}$) is set at 45° (see Figure 5).
3. The mass outflow rate normalized to the Eddington rate, where $\dot{M} = \dot{M}_{\rm out}/\dot{M}_{\rm Edd}$.
4. The ionizing X-ray luminosity ($L_{\rm X}$), which is the percentage of the 2–10 keV luminosity to the Eddington luminosity (i.e., $\%\ L_{2-10\ {\rm keV}}/L_{\rm Edd}$).
5. The photon index of the input X-ray continuum, which is set to that of the hard-X-ray power law (e.g., $\Gamma = 2.2$ for PG1448+273). As noted in Matzeu et al. (2022), a steeper Γ gives stronger absorption lines, due to the weaker ionizing hard-X-ray continuum.

Note as both the mass outflow rate and ionizing luminosity are in Eddington units and the wind radius is in gravitational units, the parameters are invariant to the black hole mass.

The above disk-wind grids were applied to the mean 2023 spectrum over the 0.3–30 keV band. The same two-component baseline continuum was applied (model (a)), where the residuals over the Fe K band reveal the wind profile of PG1448+273 in emission and absorption (Figure 6(a), $\chi^2/\nu = 764.0/622$). Initially, a single fast DW thin zone is added to the baseline model (model (b); see Table 2 for parameters). However, while this is able to account for the spectral residuals between 10 and 12 keV, at the bluewards end of the profile, it does not account for the absorption profile between 8 and 10 keV, while some of the emission remains unmodeled between 6 and 7 keV (see Figure 6(b), $\chi^2/\nu = 685.8/618$). Essentially, the absorption profile predicted by thin wind is not broad enough to account for the whole profile, as the range of terminal velocities achieved is insufficient. A second DW thin zone was then added to the model (model (c); see Table 2) and at a lower terminal velocity in order to account for the remaining residuals. This improves the fit statistic further (Figure 6(c), $\chi^2/\nu = 660.8/616$), modeling most of the lower-energy residuals, although some remain over the 7–10 keV band. Essentially this solution requires two distinct wind zones, where the fastest zone has a maximum terminal velocity of $v_\infty/c = -0.39 \pm 0.03$, modeling the bluewards extent of the profile, and a slower zone where the maximum velocity attained is $v_\infty/c = -0.23 \pm 0.03$. The parameters of the two-velocity wind are reported in Table 2 (models (b) and (c) for the two zones). Note the parameters of the faster zone do not change significantly (within errors) upon the addition of the second slower zone.

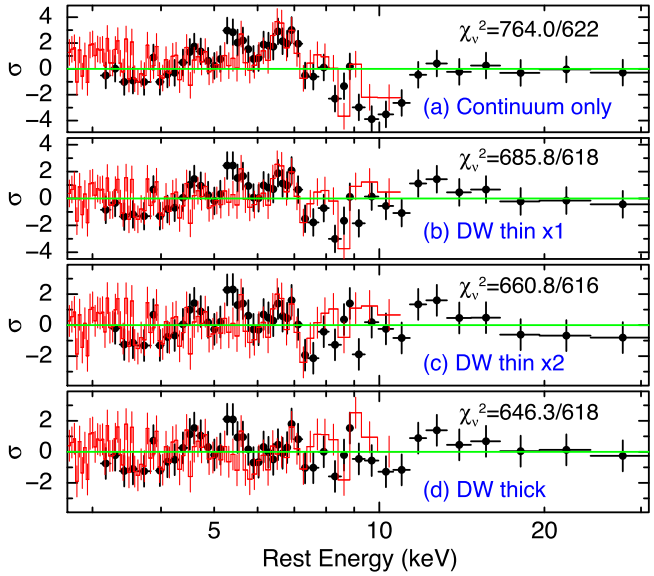

Figure 6. Residuals, in units of (data – model)/error, to the mean 2023 spectrum, plotted over the Fe K band. Panel (a) shows the residuals to the baseline continuum (no wind), panel (b) shows the case of a single DW thin grid, panel (c) corresponds to two DW thin zones, and panel (d) corresponds to the best-fit scenario of a single DW thick zone. In each case, the parameters are reported in Table 2. A geometrically thick disk wind (model (d)) best accounts for the Fe K profile in PG1448+273.

The two-zone solution requires two distinct velocity components, yet in this scenario both are assumed to be launched over the same radial range on the disk (32–48R_g). A more physical representation may correspond to the case of a geometrically thick wind, where the dispersion in terminal velocity is naturally produced over a wide range of disk radii, as $v_\infty \propto R^{-1/2}$ and $R = 32-96R_g$ in this case. The DW thick grid provides a good account of the whole Fe K-band profile (Figure 6(d)) and is also statistically the best-fit solution ($\chi^2/\nu = 646.3/618$). The best-fit wind parameters for the DW thick grid are reported in Table 2 (model (d)). Note the inclination angle of $\mu = 0.58 \pm 0.03$ (or $\theta \sim 55° \pm 2°$) is consistent with the previous modeling of the 2017 and 2022 observations (Reeves et al. 2023) and is well within the wind opening angle at 45°. In this model, a wide range of terminal velocities are realized; at the inner streamline the maximum terminal velocity is $v_{\max,\infty} = -0.43 \pm 0.03c$, while for the outer streamline the minimum terminal velocity is $v_{\min,\infty} = -0.25 \pm 0.02c$. The mean terminal velocity, averaged over all launch radii, is $<v_\infty/c> = -0.34 \pm 0.03$. This is in agreement with the outflow velocity obtained from the simple XSTAR absorber.

As a result of the wider velocity dispersion within the thick wind, it is able to model the breadth of the absorption profile, unlike the case of a single DW thin zone. This is illustrated in Figure 7, where panel (a) shows the spectrum fitted with the DW thick model and panel (b) shows the resulting Fe K profile from the wind. For the latter plot, the DW thick model (model (d)) is compared to the single DW thin model (model (b)). It is apparent that the DW thick solution predicts a substantially broader profile compared to the DW thin case, where the absorption trough is notably narrower. In addition, the DW thick model also provides a better description of the Fe K emission from the wind.

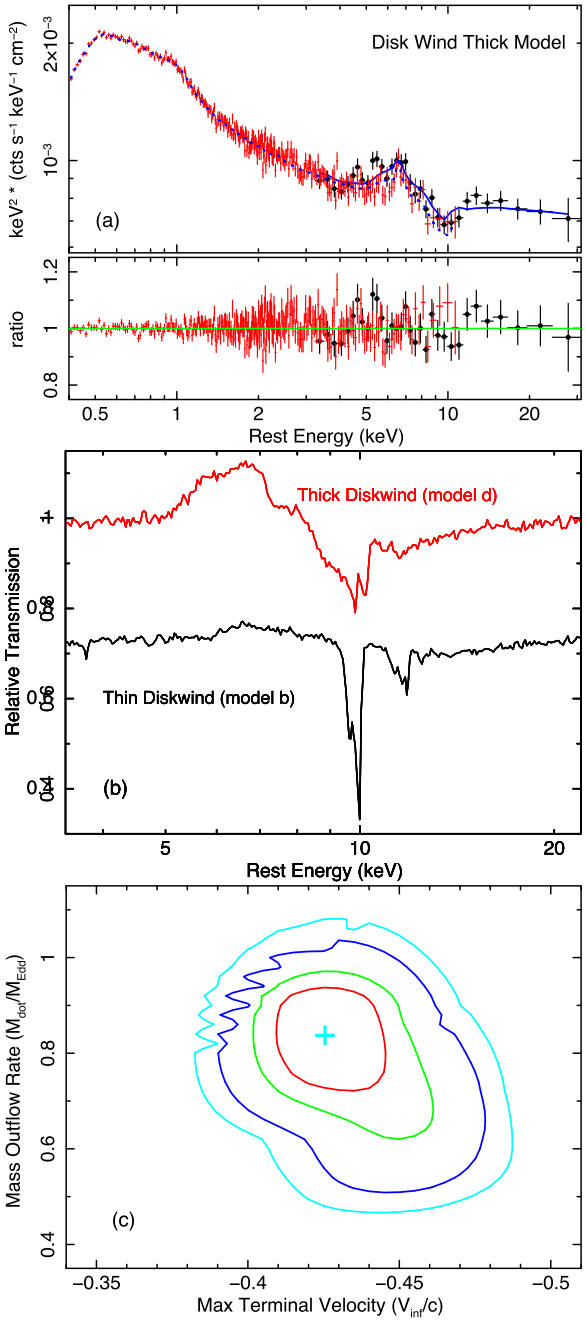

Figure 7. Results of the disk-wind modeling. Panel (a) shows the best-fit DW thick model fitted to the mean 2023 spectrum. Here, the model (folded through the instrumental responses) is shown as a solid blue line fitted to the NuSTAR data from 3 to 30 keV and as a dotted blue line to the XMM-Newton spectrum from 0.3 to 10 keV. Note the lack of strong soft-X-ray absorption. Panel (b) shows the theoretical Fe K profiles predicted from the wind for the DW thick case (red; Table 2, model (d)) vs. the DW thin case (black; Table 2, model (b)). A y-axis offset has been applied for clarity. The DW thick model produces a broader absorption-line profile due to its larger velocity shear, as well as stronger Fe K emission. Panel (c) shows the confidence contours of the mass outflow rate in Eddington units vs. the maximum terminal velocity attained by the wind for model (d). The contours represent the 68%, 90%, 99%, and 99.9% confidence levels for two interesting parameters. The mass outflow rate in PG1448+273 appears to be at nearly the Eddington rate, with a maximum terminal velocity of $v_{\max,\infty}/c = -0.43 \pm 0.03$. Note the sawtooth behavior of the outer contours is due to the finite grid resolution.

Interestingly, the mass outflow rate (normalized to Eddington) for the DW thick model is $\dot{M} = 0.84^{+0.10}_{-0.12}$, which is close to the Eddington limit. Indeed, the confidence contours of $\dot{M}$

versus $v_{\max,\infty}$ are well constrained (see Figure 7(c)) in this scenario. The mass outflow rate is also much higher than what was determined from the 2022 NuSTAR observation of PG1448+273. In particular, during the last 60 ks of that observation (slice B), a broad absorption trough was observed centered near 9 keV and the mass outflow rate was inferred to be $\dot{M} = 0.23 \pm 0.06$ (Reeves et al. 2023). The likely reason for this lower value is the adopted wind geometry, where only the thin disk-wind model was considered by Reeves et al. (2023) to model the 2022 profile. Instead, the geometrically thicker wind inferred from the higher-quality 2023 data naturally requires more mass to achieve a similar line-of-sight opacity. A comparison of the 2023 versus the 2022 epochs with the DW thick model will be considered in Section 5.

The ionizing X-ray luminosity incident upon the thick wind is found to be $L_X = 0.80\% \pm 0.08\%$, equivalent to the 2–10 keV luminosity being 0.8% of Eddington. This level of X-ray luminosity is high enough such that the most dominant ionic species is H-like iron and little absorption is predicted at soft-X-ray energies. This can also be seen from the best-fit spectrum in Figure 7(a), where the wind model is featureless at soft-X-ray energies and no significant residuals are present. As a consistency check, the above inferred ionizing luminosity can also be compared with the energetics of the AGN. The observed (absorption-corrected) 2–10 keV luminosity is $L_{2-10\,\mathrm{keV}} = 2.6 \pm 0.2 \times 10^{43}$ erg s^{-1} (see Table 2). From the reverberation black hole mass of $M_{\mathrm{BH}} = 1.01^{+0.38}_{-0.23} \times 10^7\ M_\odot$ (Hu et al. 2021), the Eddington luminosity is $L_{\mathrm{Edd}} = 1.3^{+0.5}_{-0.3} \times 10^{45}$ erg s^{-1}. Based upon these observables, the expected ratio of the 2–10 keV to Eddington luminosity is $2.0\% \pm 0.6\%$. Within the uncertainties, this is comparable (within a factor of 2) to the values inferred from the disk-wind modeling; here, $L_X = 0.80\% \pm 0.8\%$ for the DW thick case and $L_X = 1.4^{+0.3}_{-0.2}\%$ for the DW thin case. This suggests the disk wind is just slightly underionized when compared to the observed 2–10 keV luminosity.

4.2. Modeling with the Relativistic WINE model

Here, we apply the WINE model of Luminari et al. (2018) to provide an alternative parameterization of the wind. The WINE model was originally developed to model the emission profiles resulting from disk winds, motivated by the P Cygni profile observed in PDS 456 (Nardini et al. 2015). The model has since been extended to self-consistently calculate the wind absorption and has been applied to the wind in the 2017 XMM-Newton observation of PG1448+273 (Laurenti et al. 2021) and to the variable wind of NGC 2992 (Luminari et al. 2023). A forthcoming detailed description of the updated model can be found in Luminari et al. (2024).

In summary, the wind geometry is a conical outflow (see Figure 1; Luminari et al. 2018, 2024), with a half-opening angle of θ_{out} with respect to the polar axis. It is launched at an inner radius of R_0 (in Schwarzschild units of $R_s = 2GM/c^2$), with an initial (innermost) ionization parameter of ξ_0. The wind absorption is then integrated over a succession of thin shells versus radius as calculated by XSTAR, while the wind emission is integrated over all solid angles and radii. Special-relativistic effects are accounted for as described in Luminari et al. (2020, 2021), including the relativistic deboosting of the continuum as seen by gas expanding radially outwards. The latter effect is important in PG1448+273 given the large velocities inferred from the Fe K absorption profile. In order to calculate the resultant line profiles, a wind density profile of $n(r) = n_0(R/R_0)^{-1}$ is adopted along with a radial velocity profile of $v(r) = v_0(R/R_0)^{-\frac{1}{2}}$; here, n_0 and v_0 are the inner number density and velocity at the initial launch radius R_0. Note the choice of radial profiles is consistent with a momentum-conserving wind (e.g., Faucher-Giguère & Quataert 2012), while the velocity profile describes a ballistic trajectory deaccelerating under gravity.

To fit the PG1448+273 spectrum, the absorption and emission spectra from the WINE model were calculated in the form of two XSPEC multiplicative tables, which modify the same baseline continuum as described earlier. The output parameters for spectral fitting are the inner ionization ($\log \xi_0$), inner velocity (v_0), inner radius (R_0), column density (N_{H}), and half-opening angle (θ_{out}). The first three parameters are assumed to be equal in both absorption and emission, except for the column density, which may differ along the line of sight versus (on average) across the whole wind. The opening angle is only relevant to the wind emission, as it is calculated over all angles. Note that the inclination between the line of sight and the wind symmetry axis is fixed to 0°, since it cannot be constrained by the data, unlike the disk-wind model, which adopts a biconical geometry with a minimum opening angle of 45° (Figure 5). In WINE, this angle corresponds to a disk observed face-on through a conical, polar wind.

The WINE model produces a good fit to the PG1448+273 spectrum and in particular over the Fe K band (see Figure 8), with a similar overall fit statistic as per the DW thick case in Section 4.1, with $\chi^2/\nu = 656.3/618$. The fit parameters of the WINE model are listed in Table 3, where the maximum wind launch velocity is $v_0/c = -0.50 \pm 0.02$, just slightly higher than the equivalent maximum terminal velocity obtained by the DW thick model. Note that in the best-fit solution, the minimum wind velocity is $v_{\min} = -0.21c$, while the mass-averaged velocity is $v_{\mathrm{avg}} = -0.325c$. This range of velocity is consistent with what was derived from the DW thick grid (model (d), Table 2).

The launch radius is a variable parameter in the WINE model and the best-fit value is $R_0 = 16.3^{+2.6}_{-1.8} R_s$. This is consistent with the inner launch radius (of $32R_g$ or $16R_s$) assumed in the disk-wind models in Section 4.1 and demonstrates that such fast winds are likely to be launched from the innermost regions of the accretion disk. The absorption column density is $N_{\mathrm{H,abs}} = 0.57 \pm 0.06 \times 10^{24}$ cm^{-2}, while the emitter column is higher, with $N_{\mathrm{H,emiss}} = 1.7 \pm 0.3 \times 10^{24}$ cm^{-2}. This may occur if the wind is nonuniform, for instance if the column density is higher at larger θ toward the equatorial direction; this is the case for the disk-wind models (higher N_{H} at larger θ). Finally, from the wind emission, the opening angle is constrained to be $\theta_{\mathrm{out}} > 72°$, which corresponds to a lower limit on the wind geometric covering fraction of $f_{\mathrm{cov}} = 1 - \cos(\theta_{\mathrm{out}}) > 0.69$. Indeed, the larger the opening angle is, the stronger the wind emission will be.

The innermost density at the launching point of wind is given by the definition of the ionization parameter, where $\xi_0 = L'_{\mathrm{ion}}/n_0 R_0^2$; here, L'_{ion} is the 1–1000 Rydberg ionizing luminosity corrected for the deboosting of the continuum radiation. Following Luminari et al. (2020, 2023), the deboosted luminosity is given by $L'_{\mathrm{ion}} = \left(\frac{1-v}{1+v}\right)^{\frac{2+\Gamma}{2}} L_{\mathrm{ion}}$, where Γ is the photon index and this also accounts for the redshift of the continuum as seen by the wind. Extrapolation of the best-fit baseline continuum model from 1 to 1000 Rydberg gives

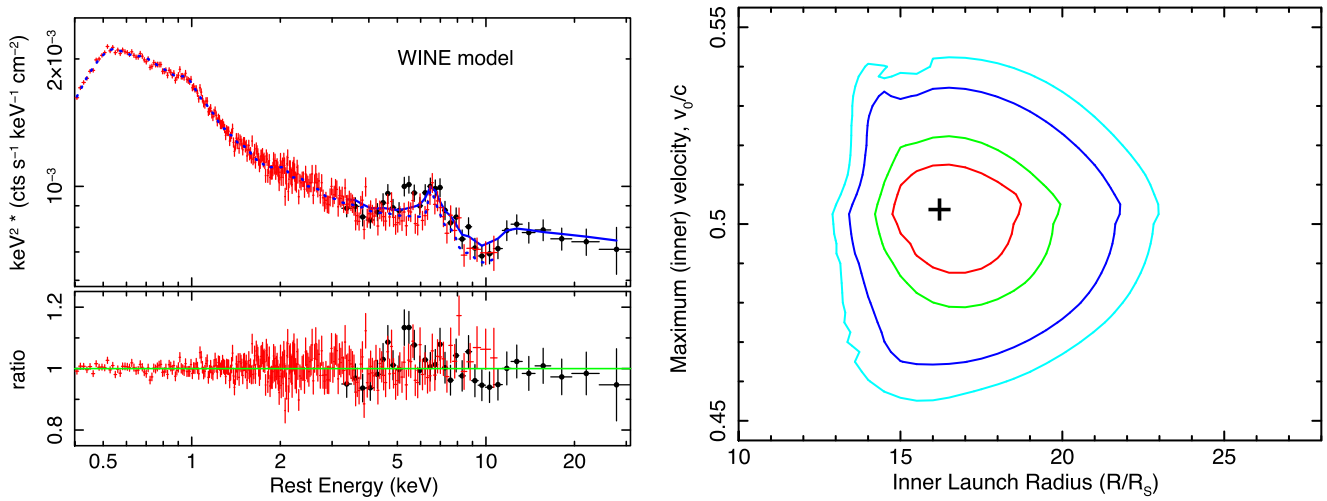

Figure 8. Results of modeling the mean 2023 PG1448+273 spectrum with the relativistic WINE wind model (Luminari et al. 2018). The left panel shows the best-fit fluxed spectrum, where the folded counts spectrum has been multiplied twice by energy. The WINE model is shown as a blue line (solid for NuSTAR, dotted for EPIC-pn) and reproduces well the Fe K absorption and emission profile, as is seen by the data/model residuals. The right panel shows the 68%, 90%, 99%, and 99.9% confidence intervals of the maximum wind velocity (v_0/c, at the innermost radius) vs. the inner launch radius (R_0), where the latter is in units of the Schwarzschild radius (R_s). In the best-fit scenario, the wind is launched from a radius of $R_0 = 16R_s$ at a maximum velocity of $0.5c$.

Table 3
Results of Fitting the WINE Model to the 2023 Spectrum

Parameter	Value
Fitted Parameters:	
Absorption column, $N_{H,abs}/10^{24}$ cm^{-2}	0.57 ± 0.06
Ionization, $\log(\xi_0/\mathrm{erg\ cm\ s^{-1}})$	5.58 ± 0.04
Inner velocity, v_0/c	0.50 ± 0.02
Inner radius, R_0/R_s	$16.3^{+2.6}_{-1.8}$
Emission column, $N_{H,emiss}/10^{24}$ cm^{-2}	1.7 ± 0.3
Half-opening angle, θ_{out}	$>72°$
Photon index, Γ	2.14 ± 0.02
Fit statistic, χ^2/ν	656.3/618
Derived Parameters:	
Deboosted luminosity, $L'_{ion}/10^{43}$ erg s^{-1}	2.0 ± 0.2
Inner density, $n_0/10^{10}$ cm^{-3}	$2.1^{+0.9}_{-0.7}$
Covering fraction, f_{cov}	>0.69
Mass outflow rate, $\dot{M}_{out}/M_\odot$ yr^{-1}	$0.14^{+0.05}_{-0.04}$[a]
Normalized outflow rate, $\dot{M}_{out}/\dot{M}_{Edd}$	$0.61^{+0.23}_{-0.17}$[a]

Note.
[a] The minimum mass outflow rate, corresponding to $f_{cov} = 0.69$.

$L_{ion} = 2.0 \pm 0.2 \times 10^{44}$ erg s^{-1}, while from the above the continuum is deboosted by a factor of 10 for $v_0/c = 0.5$ and $\Gamma \approx 2.2$. Thus, the resultant deboosted luminosity is $L'_{ion} = 2.0 \pm 0.2 \times 10^{43}$ erg s^{-1} and the innermost density is $n_0 = 2.1^{+0.9}_{-0.7} \times 10^{10}$ cm^{-3}.

From this and the best-fit parameters in Table 3, the mass outflow rate is calculated as per Laurenti et al. (2021):

$$\dot{M}_{out} = 2\,\mu m_p \int_0^{2\pi} \int_0^{\theta_{out}} \int_{r_0}^{r_1} n(r) v(r) r \sin\theta\ dr\ d\theta\ d\phi, \quad (3)$$

where μ and m_p are the mean atomic mass per proton and the proton mass, respectively. The wind outer radius, r_1, is calculated analytically from the integral of the density to calculate the absorption column density, while the factor of 2 arises from summing both hemispheres of the wind. From this integral and the radial velocity and density profiles as above, the mass outflow rate is determined to be $\dot{M}_{out} = 0.21^{+0.08}_{-0.06} f_{cov}\ M_\odot$ yr^{-1}. The lower limit of $\theta_{out} > 72°$ then yields $f_{cov} > 0.69$. Thus, the minimum mass outflow rate is $\dot{M}_{out} = 0.14^{+0.05}_{-0.04}\ M_\odot$ yr^{-1}. For an accretion disk efficiency of $\eta = 0.1$ and the black hole mass of PG1448+273 (Hu et al. 2021), this corresponds to a normalized rate of $\dot{M}_{out}/\dot{M}_{Edd} = 0.61^{+0.23}_{-0.17}$ (or $\dot{M}_{out}/\dot{M}_{Edd} = 0.91^{+0.35}_{-0.26}$ for $f_{cov} = 1$). This is consistent with the mass outflow rate inferred by the disk-wind model in Section 4.1.

5. Wind Variability

To test for any wind variability, the DW thick model in Section 4.1 was applied to the four individual 2023 sequences (OBS 1, 2b, 3, and 4), including both the XMM-Newton and NuSTAR spectra over the 0.3–30 keV band. Note the short (dipping) OBS 2a segment was not included, as its net exposure (6 ks with EPIC-pn) is too short to derive any useful wind constraints, although overall its spectrum is harder, with $\Gamma = 1.93 \pm 0.07$. The wind parameters in each case are reported in Table 4. The results are very similar to the mean spectrum, with no significant variation in the maximum terminal velocity of the wind, i.e., from $v_{max,\infty}/c = -0.43 \pm 0.04$ (OBS 4) to $v_{max,\infty}/c = -0.48 \pm 0.04$ (OBS 2b). Neither is there any strong variability in the X-ray flux across the epochs. The mass outflow rate also remains steady and close to Eddington across the four epochs, ranging from $\dot{M} = 0.73 \pm 0.19$ (OBS 1) to $\dot{M} = 1.20^{+0.15}_{-0.20}$ (OBS 2b). This implies there is no significant intrinsic wind variability across the 40 day campaign.

We also compare the properties of the wind in the 2023 mean spectrum with those in the 2022 NuSTAR observations (Reeves et al. 2023). Here, we apply the DW thick model to both epochs for consistency. As described in Reeves et al. (2023), the 2022 NuSTAR observation was split into two slices (slice A and slice B) either side of a factor of 2 drop in flux. The slice A spectrum covered the first 190 ks in duration of the 2022 NuSTAR observation, where the source is brightest

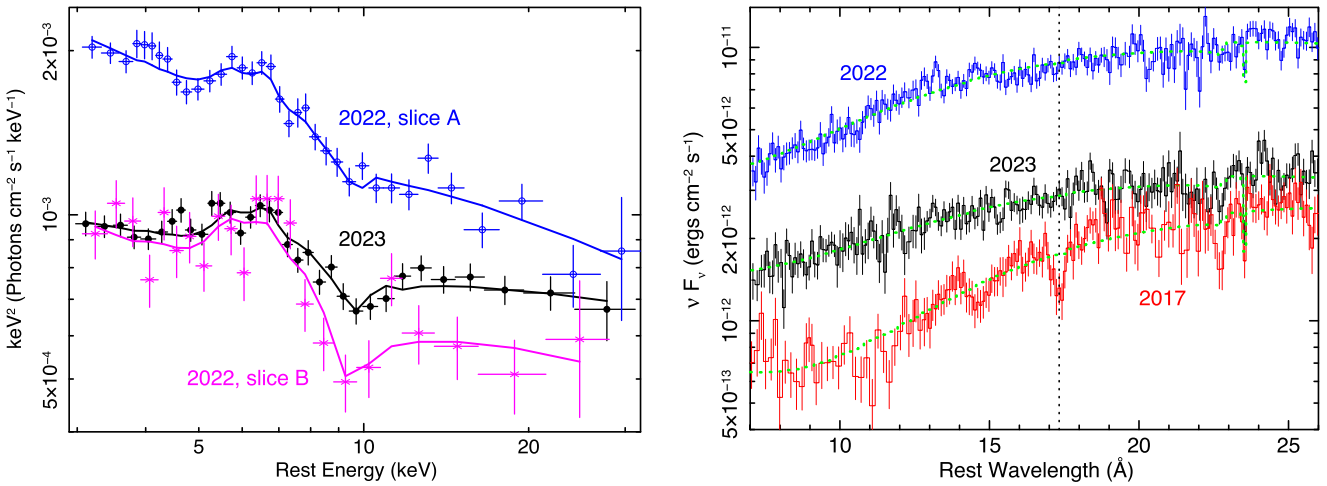

Figure 9. Comparison of the PG1448+273 spectra over different epochs from 2017 to 2023. The left panel shows the the mean 2023 vs. the 2022 A (slice A) and 2022 B (slice B) NuSTAR spectra, fitted with the thick disk-wind model in each case. The spectral differences between each epoch can be accounted for via changes in ionization through the variations in X-ray luminosity, as well as in photon index. Note there was no NuSTAR observation in 2017. The right panel shows the comparison of the 2017, 2022, and 2023 RGS spectra. Significant soft-X-ray wind absorption was only detected in the low-flux 2017 spectrum, in the form of a blueshifted O VIII Lyα line, as marked by the dotted vertical line.

Table 4
Results of Spectral Fitting to OBS 1–4

Parameter	OBS 1	OBS 2b	OBS 3	OBS 4
Photon index, Γ	2.18 ± 0.03	2.11 ± 0.04	2.15 ± 0.04	2.22 ± 0.04
Power-law normalization ($N_{\rm PL}$)[a]	1.28 ± 0.06	1.24 ± 0.08	1.07 ± 0.07	1.38 ± 0.09
2–10 keV flux ($F_{2-10\ \rm keV}$)[b]	2.22	2.17	1.82	2.16
Mass outflow rate ($\dot{M}_{\rm out}/\dot{M}_{\rm Edd}$)	0.73 ± 0.19	$1.20^{+0.15}_{-0.20}$	$1.05^{+0.18}_{-0.20}$	$0.90^{+0.13}_{-0.20}$
Ionizing luminosity (% $L_{2-10\ \rm keV}/L_{\rm Edd}$)	0.80 ± 0.13	0.80[c]	0.80[c]	0.80[c]
Maximum terminal velocity ($v_{\rm max,\infty}/c$)	-0.46 ± 0.03	-0.48 ± 0.04	-0.44 ± 0.03	-0.43 ± 0.04
Minimum terminal velocity ($v_{\rm max,\infty}/c$)	-0.27 ± 0.02	-0.28 ± 0.03	-0.25 ± 0.02	-0.25 ± 0.03
Inclination ($\mu = \cos\theta$)	0.58 ± 0.04	0.58[c]	0.58[c]	0.58[c]
Fit statistic (χ^2/ν)	776.9/706	523.9/527	588.5/582	453.7/442

Notes.
[a] Power-law normalization ($\times\ 10^{-3}$ photons cm^{-2} s^{-1} keV^{-1} at 1 keV).
[b] Observed 2–10 keV flux, in units of $\times\ 10^{-12}$ erg cm^{-2} s^{-1}.
[c] Denotes parameter is tied within the model.

($F_{2-10\ \rm keV} = 4.7 \times 10^{-12}$ erg cm^{-2} s^{-1}) and the spectrum was relatively featureless. Then in the last 60 ks of the observation, the flux dropped by a factor of 2, reaching a similar level to what is observed in the mean 2023 observation and where a strong absorption trough emerged between 8 and 12 keV.

The three NuSTAR spectra (2022 A, 2022 B, and 2023) were then fitted with the DW thick grid (model (d)), adopting a simple power-law continuum covering the 3–30 keV hard-X-ray band. These are shown in Figure 9 (left panel), while the results are reported in Table 5. Given the factor of 2 difference in luminosity between the brighter 2022 A spectrum versus the 2022 B and 2023 spectra, the ionizing luminosity ($L_{\rm X}$) was set to be a factor of 2 higher for the former case. Similar to what was found above, the mass outflow rate is consistent between all three epochs, and thus any difference in the opacity of the wind at Fe K simply arises from the higher luminosity of the 2022 A spectrum, which serves to increase the wind ionization. Thus, across the 2022 and 2023 epochs, no intrinsic variations in the wind parameters appear to be observed, and they are consistent with a constant terminal velocity and mass outflow rate. The spectral changes can mainly be explained by variations in the X-ray luminosity, along with changes in the photon index.

Table 5
Comparison between the 2023 and 2022 NuSTAR Spectra

Parameter	2023	2022 A	2022 B
Γ	2.16 ± 0.03	2.42 ± 0.04	2.31 ± 0.09
$N_{\rm PL}$ [a]	1.29 ± 0.08	3.67 ± 0.22	1.53 ± 0.23
$F_{2-10\rm keV}$ [b]	2.38 ± 0.15	4.71 ± 0.28	2.25 ± 0.34
$\dot{M}_{\rm out}/\dot{M}_{\rm Edd}$	0.91 ± 0.22	$0.79^{+0.21}_{-0.19}$	$0.92^{+0.32}_{-0.31}$
$\%L_{2-10\ \rm keV}/L_{\rm Edd}$	$0.58^{+0.13}_{-0.11}$	1.16[c]	0.58[c]
$v_{\rm max,\infty}/c$	-0.42 ± 0.02	-0.42[c]	0.42[c]
$\mu = \cos\theta$	0.61 ± 0.03	0.61[c]	0.61[c]
χ^2/ν	55.8/62	103.0/104	26.3/21

Notes.
[a] Power-law normalization ($\times\ 10^{-3}$ photons cm^{-2} s^{-1} keV^{-1}).
[b] Flux in units of $\times\ 10^{-12}$ erg cm^{-2} s^{-1}.
[c] Denotes parameter is tied within the model.

Finally, the soft-X-ray wind properties are compared from the respective XMM-Newton RGS epochs. The mean 2023

RGS spectrum versus the 2022 and 2017 epochs is shown in Figure 9 (right panel). The 2023 RGS spectrum is virtually featureless, with no strong emission or absorption within the 3σ level, and it can be fitted with the baseline continuum model of Section 4 with an acceptable fit statistic ($\chi^2/\nu = 242.8/218$). This is in contrast with the 2017 low-X-ray flux epoch, where significant soft-X-ray wind features were observed from O VIII in particular; see Kosec et al. (2020) and Reeves et al. (2023). The vertical line on Figure 9 marks the position of the strong and broadened O VIII Lyα absorption line in the 2017 spectrum, occurring at $\lambda = 17.3 \pm 0.1$ Å (rest frame) and blueshifted by $\sim 0.1c$ with respect to the expected wavelength of 18.9 Å. Indeed, in Reeves et al. (2023) a disk-wind model with this velocity could account for both the O VIII and Fe K-band absorption in the 2017 epoch. In contrast, no such soft-X-ray outflow is found in either the 2023 or the bright 2022 epoch, with upper limits on the equivalent width of the O VIII line of <1.4 eV and <1.8 eV for 2023 and 2022, respectively, versus an equivalent width of 5.1 ± 1.8 eV in 2022. This result is consistent with the lack of soft-X-ray absorption from the 2023 disk wind modeling and suggests the wind is of an overall higher ionization compared to the low-flux 2017 epoch.

6. Discussion

NuSTAR and XMM-Newton observations of PG1448+273 in 2023 have revealed a remarkable UFO, with one of the most extreme blueshifts measured to date among UFO sources. The Fe K-band absorption can be parameterized by a simple Gaussian line profile, with a centroid energy of 9.8 ± 0.4 keV, which, if it is associated to Fe XXVI Lyα, implies an average blueshift of $v/c = -0.33 \pm 0.02$ after accounting for the special-relativistic correction on the velocity along the line of sight. This is also consistent with the mean velocity obtained from the best-fitting thick disk-wind model, of $<v/c> = -0.34 \pm 0.02$, as is described in Section 4.1 (see Table 2, model (d)). The velocity width of the Fe K absorption profile is also pronounced, where $\sigma = 1.1^{+0.5}_{-0.4}$ keV, equivalent to $\sigma_v \sim 0.1c$. This implies a considerable velocity shear, as a result of a range of velocities intercepted along our sightline through the wind. This can be accounted for by the geometrically thick disk-wind model, launched over a wide range in radii, where the terminal velocity reaches a maximum value of $v_{\rm max,\infty} = -0.43 \pm 0.03c$ at the inner edge of the wind, with a minimum velocity of $v_{\rm min,\infty} = -0.25 \pm 0.02c$ at the outermost radius. The velocity dispersion of $\Delta v = \pm 0.1c$ within the wind is consistent with the Gaussian line width as measured above. Similar results were also found for the relativistic WINE model, where the maximum wind velocity was found to be $v_0/c = -0.50 \pm 0.02$. From the wind emission, the half-opening angle of the wind was constrained by WINE to be $\theta_{\rm out} > 72°$ and covering $>2\pi$ steradian solid angle.

6.1. Comparison with Other Winds

Thus, the wind profile in PG1448+273 resembles the P Cygni–like profile in PDS 456 (Nardini et al. 2015), with broad structure due to emission and absorption from a wide-angle outflow. The outflow velocity in PG1448+273 appears to be at the higher end of what has been measured in the prototype UFO in PDS 456, which typically spans the range between $v/c = 0.25$ and 0.35 (Matzeu et al. 2017). Note that in some epochs the fastest outflow component in PDS 456 can also reach values exceeding $0.4c$ (Reeves et al. 2018). A similarly high terminal velocity of $v_\infty = -0.38 \pm 0.02c$ has been reported based upon the disk-wind modeling of the similarly luminous QSO IRAS F11119+3257 (Lanzuisi et al. 2024). Such velocities may appear to be more commonplace in the most luminous AGNs at the peak of the quasar epoch at high redshifts (see Chartas et al. 2021, and references therein).

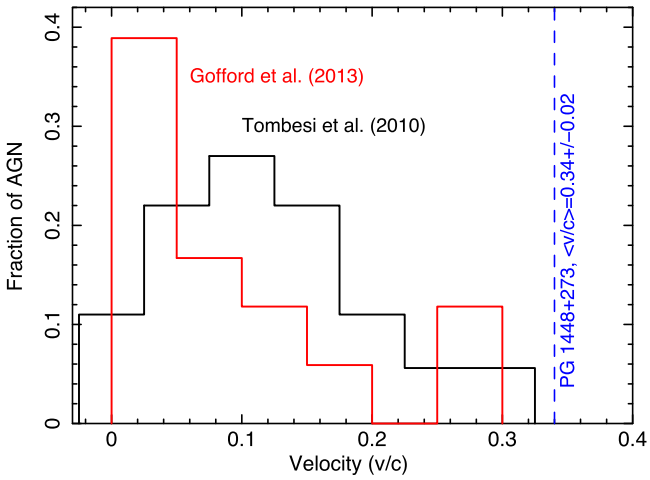

Figure 10. The distribution of wind velocities obtained from two samples of nearby UFOs (Tombesi et al. 2010; Gofford et al. 2013) vs. the wind velocity in PG1448+273 observed in 2023. The mean velocity in Tombesi et al. (2010) is close to $-0.1c$, while the median velocity of the Gofford et al. (2013) sample is $-0.056c$, both of which are considerably lower than the average terminal velocity of $<v/c> = -0.34 \pm 0.02$ attained by the PG1448+273 wind as measured by the DW thick model. Note an even higher value of $v_\infty/c = -0.43 \pm 0.03$ was found for the maximum terminal velocity. Neither of the Tombesi et al. (2010) and Gofford et al. (2013) samples contains a wind exceeding $>0.3c$ in comparison.

The velocity measured in PG1448+273 is much higher than what has been measured in samples of other nearby (e.g., $z < 0.1$) AGNs (Tombesi et al. 2010; Gofford et al. 2013). For illustration, Figure 10 compares the mean disk-wind velocity measured in PG1448+273 with the distributions of velocities obtained from the XMM-Newton and Suzaku UFO samples of Tombesi et al. (2010) and Gofford et al. (2013), respectively. In the Tombesi et al. (2010) sample, the mean velocity is $v/c \approx -0.1$, while the distribution of Gofford et al. (2013) is skewed to lower velocities, with a median velocity of $v/c = -0.056$. There are no AGNs across either sample where the outflow velocity exceeds $-0.3c$. This is also similar to what was found in Igo et al. (2020), where the absorption lines were detected through the excess variance spectra of nearby AGNs. Likewise, a similar range of velocity was also obtained in the SUBWAYS sample of Matzeu et al. (2023), which consists of a sample of QSOs at intermediate redshifts ($z = 0.1-0.4$).

Furthermore, the equivalent width of the Fe K absorption line in PG1448+273, with EW $= -435^{+150}_{-190}$ eV, is much higher than those in other nearby AGNs; for instance, in the Gofford et al. (2013) sample the highest equivalent width is 150 eV with a mean of 40 eV (see, e.g., their Figure 7), while similar values were also reported by Tombesi et al. (2010). Thus, among these local AGNs, PG1448+273 has one of the highest reported outflow velocities, while the equivalent width is substantially higher. This implies a more powerful wind compared to the predominantly broad-lined Seyfert 1 galaxies studied by Tombesi et al. (2010) and Gofford et al. (2013). In this regard, PG1448+273 resembles the UFOs reported in

other NLS1s, with velocities at the higher range of the AGN distribution from 0.2 to 0.3c and where the absorption features have higher optical depths, e.g., IRAS 13224−3809 (Parker et al. 2017; Chartas & Canas 2018; Pinto et al. 2018), 1H 0707 −495 (Hagino et al. 2016; Kosec et al. 2018), I Zw 1(Reeves & Braito 2019), and WKK 4438 (Jiang et al. 2018).

It appears plausible that the high accretion rates in NLS1s are more conducive for driving a more powerful wind, as they accrete at high Eddington ratios, have strong UV emission, and generally have steep X-ray spectra with weak hard-X-ray emission (Giustini & Proga 2019). The latter effect is important, as steep, weak hard-X-ray spectral energy distributions will tend to produce deeper X-ray wind features due to the gas being less ionized. This was illustrated in the disk-wind simulations of Matzeu et al. (2022, see their Figure 3), where the Fe K absorption profile becomes progressively stronger as the power-law photon index increases from $\Gamma = 1.6$ to $\Gamma = 2.4$, with the equivalent widths increasing to up to hundreds of eV in the steepest sources. It is also consistent with the observed properties of PG1448+273, which has an intrinsically steep hard-X-ray spectrum ($\Gamma = 2.2-2.4$) and a relatively low inferred ratio of X-ray to bolometric luminosity, e.g., $L_{2-10\,\mathrm{keV}}/L_{\mathrm{Edd}} \approx 1\%$.

6.2. The Variable Wind of PG1448+273

The velocities of UFOs have been shown to vary in several AGNs. Some of the most notable cases reported to date occur in APM 08279+5255 (Saez & Chartas 2011), PDS 456 (Matzeu et al. 2017), IRAS 13224−3809 (Chartas & Canas 2018), and MCG−03−58−007 (Braito et al. 2021, 2022). PG1448+273 also appears to exhibit substantial variability in its terminal velocity across epochs, which may vary by up to a factor of 4. XMM-Newton observations of PG1448+273 in 2017 caught the AGN in a low-flux state and where the Fe K absorption trough appeared at a much lower centroid energy of 7.5 keV (Kosec et al. 2020; Laurenti et al. 2021; Reeves et al. 2023), and implying a mean wind velocity of ≈0.1c (Reeves et al. 2023). In contrast, in the brighter 2022 and 2023 observations, the absorption trough is measured above 9 keV, while all of these later, brighter epochs are consistent with the thick disk wind attaining a maximum terminal velocity of ≈0.4c. The higher velocities in the 2022–23 epochs versus 2017 might be connected to the higher X-ray flux in the later observations.

The 2017 epoch of PG1448+273 may also be unusual, as it occurred during a pronounced X-ray dipping period. This was observed from the Swift monitoring during this period (Laurenti et al. 2021), where the X-ray flux dropped by up to an order of magnitude compared to the optical and UV flux. This decrease may have had a substantial effect on the wind properties, with the wind being substantially slower and also of lower ionization. The latter effect is illustrated by the multi-epoch comparison of the RGS spectra (Figure 9, right panel), where a deep trough was present in the 2017 spectrum due to O VIII Lyα at a velocity of $-0.1c$, as reported in Kosec et al. (2020) and Reeves et al. (2023), but which is absent during the brighter 2022–23 periods. Further monitoring with XMM-Newton and NuSTAR will help to reveal whether PG1448 +273 continues to maintain the large velocity measured in 2022–23, or whether the AGN wind reacts to any prolonged decreases in luminosity via its ionization and velocity as in the 2017 epoch.

Table 6
Outflow Energetics of PG1448+273 in 2023

Parameter	Value
$<v_\infty/c>$[a]	-0.34 ± 0.02
$\dot{M}$[b]	0.84 ± 0.12 ($0.19^{+0.11}_{-0.06}\,M_\odot$ yr^{-1})
$\dot{E}$[c]	0.53 ± 0.09 ($6.8^{+4.0}_{-2.4} \times 10^{44}$ erg s^{-1})
$\dot{p}$[d]	3.0 ± 0.5 ($1.3^{+0.8}_{-0.5} \times 10^{35}$ dyne)

Notes.
[a] Mean terminal velocity of the wind.
[b] Mass outflow rate in Eddington units, as per Table 2 (absolute value in parenthesis).
[c] Outflow kinetic power in Eddington units.
[d] Outflow momentum rate in Eddington units.

6.3. Kinematics and Wind-driving Mechanisms

Here, we estimate the kinematics of the disk wind in PG1448 +273 from the 2023 observations. The mass outflow rates and terminal velocities derived from the disk-wind modeling in Section 4.1 (DW thick case) are adopted (Table 2, model (d)). Here, the resultant mass outflow rate ($\dot{M}$) is expressed in Eddington units. To provide a more conservative estimate of the energetics, the average terminal velocity attained by the wind is adopted (i.e., $v/c = -0.34 \pm 0.02$) rather than the maximum terminal value, which is achieved at the innermost edge of the streamline. The kinetic power in Eddington units ($\dot{E}$) is subsequently

$$\dot{E} = \frac{L_{\mathrm{kin}}}{L_{\mathrm{Edd}}} = \frac{1}{\eta}(\gamma - 1)\dot{M}, \tag{4}$$

where γ is the Lorentz factor and η is the accretion efficiency (and where $\eta = 0.1$ is adopted here). The corresponding wind momentum thrust in Eddington units is subsequently

$$\dot{p} = \frac{\dot{p}_{\mathrm{out}}}{\dot{p}_{\mathrm{Edd}}} = \frac{1}{\eta}\dot{M}\frac{v}{c}. \tag{5}$$

The outflow energetics of PG1448+273 in 2023 are listed in Table 6, while consistent results are also obtained with the WINE model. Note the absolute values are included in parenthesis, which take into account the uncertainties on the black hole mass measured by Hu et al. (2021). As a result of the large wind velocity and the high mass outflow rate determined by the disk-wind modeling, as well as the wide-angle nature of the wind, the kinetic power during the 2023 observations reaches about 50% of the Eddington luminosity. This is at least an order of magnitude higher than what is postulated to be significant in terms of mechanical feedback in the host galaxy (Hopkins & Elvis 2010). Furthermore, the normalized momentum rate (compared to Eddington) also exceeds unity, i.e., $\dot{p}_{\mathrm{wind}}/\dot{p}_{\mathrm{Edd}} \approx 3$. In contrast, a ratio of about 1 is predicted for black hole winds (e.g., King & Pounds 2003), arising from the average single-electron scattering limit for the radiation field in a moderately Compton-thick wind ($N_{\mathrm{H}} \sim 10^{24}$ cm^{-2}). This is also generally higher than the observed values derived from UFO samples (e.g., Tombesi et al. 2013; Gofford et al. 2015).

We also compare the mass outflow rate computed by the disk-wind (DW thick case) and WINE models with that obtained by the more simple XSTAR model in Section 4. Here, the general form of the mass outflow rate is adopted, according

to Tombesi et al. (2013) and Gofford et al. (2015), where

$$\dot{M} = 4\pi f_{\rm cov}\,\mu {\rm m_p} N_{\rm H} v_{\rm out} R. \quad (6)$$

Here, $\mu {\rm m_p}$ is the average baryonic particle mass ($\mu = 1.27$ for cosmic abundances) and $f_{\rm cov}$ is the geometrical covering, while $N_{\rm H} = 6.2^{+1.5}_{-2.1} \times 10^{23}$ cm^{-2} and $v/c = -0.34 \pm 0.02$ from the XSTAR fits. A covering of $f_{\rm cov} = 0.7$ is adopted to provide a like-for-like comparison with the WINE model, while likewise a launch radius of $R = 16R_{\rm S}$ is used. For these values, then subsequently $\dot{M}_{\rm out} = 0.09 \pm 0.03\ M_{\odot}$ yr^{-1}, or equivalently $\dot{M}_{\rm out}/\dot{M}_{\rm Edd} = 0.40 \pm 0.12$ (for $\eta = 0.1$). The latter value is similar to, but somewhat lower than, the values computed by the disk-wind model (Table 2, DW thick case) and WINE (Table 3). On the other hand, the XSTAR value may be somewhat underestimated, as it does not account for special-relativistic effects and the deboosting of the continuum as seen by the wind, as is calculated in Luminari et al. (2020).

Overall, it may be difficult to accelerate and sustain such a fast powerful wind by continuum (i.e., Thomson) radiation pressure alone, even for an Eddington-limited AGN. The maximum possible wind velocity in the radiative case will also be limited by special-relativistic effects. Here, the ability of radiation alone to drive a wind velocity as high as $-0.4c$ will be further restricted, due to the nonnegligible deboosting of the radiation field as received by the outflowing gas (Luminari et al. 2020, 2021).

In contrast, magnetohydrodynamical (MHD) winds are not limited by such effects and potentially can drive Fe K winds from the innermost accretion disk to velocities as high as $-0.6c$ (Fukumura et al. 2010). As illustrated in Figure 3 in Fukumura et al. (2010), the most favorable conditions occur in AGNs with steep X-ray spectra (either in $\alpha_{\rm ox}$ or Γ). The relative paucity of hard-X-ray photons then prevents overionization of either Fe XXV or Fe XXVI in the innermost wind regions, where the fastest part of the wind is launched. Such models are able to reproduce the fast wind in PDS 456, attaining a maximum wind velocity of up to $-0.39c$ in that case (Fukumura et al. 2018). The large velocity width of the absorption profile in PG1448+273 is reminiscent of the profiles predicted by MHD winds, especially for steep Γ sources due to the more favorable ionization conditions (Fukumura et al. 2018, 2022). This is as a result of the large range in radii over which the wind is launched on the disk, where $v_{\infty} \propto R^{-1/2}$. In both the MHD and radiation cases (Matzeu et al. 2022), a high accretion rate with respect to Eddington is also beneficial, as this will increase the outflow density, further lowering the wind ionization. Thus, in the high-accretion-rate NLS1s, both the properties of the incident radiation field and MHD processes can play an important part in accelerating and sustaining disk winds to such high velocities.

However, the large outflow rates may be at least in part mitigated by a lower geometrical covering of the gas. The broad emission component determines the overall extent of the wind. Yet, if part of the emission profile is formed by a relativistic accretion disk line (see, e.g., Parker et al. 2022 or Middei et al. 2023), then the restrictions on the covering fraction could be relaxed. This would help to reconcile the derived mass outflow rate with UV line-driven wind simulations. For example, in Nomura et al. (2020), the mass outflow rates can approach 50% of Eddington as the Eddington limit is reached; such rates are largely consistent with what is observed here. As demonstrated by Mizumoto et al. (2021), UV line-driven winds can be inhomogeneous and produce a wide range in observed outflow velocities as a result of the in situ acceleration of the wind. The strong UV to soft-X-ray excesses in NLS1s such as PG1448+273, in contrast to AGNs with higher masses and low Eddington ratios, may also enhance a line-driven wind. Furthermore, in the mildly super-Eddington regime, powerful yet clumpy winds can even be formed by continuum (i.e., Thomson) radiation pressure alone (Takeuchi et al. 2013). The properties of these winds, whether they are clumpy and/or inhomogeneous, will be soon revealed by the Resolve calorimeter on XRISM (Tashiro et al. 2020), which thanks to its high spectral resolution will accurately probe the velocity field of the outflowing gas.

Acknowledgments

J.R. and V.B. acknowledge financial support through NASA grant Nos. 80NSSC22K0474 and 80NSSC23K1467. D.P. acknowledges financial support from the CNES french spatial agency. A.L. acknowledges support from the HORIZON-2020 grant "Integrated Activities for the High Energy Astrophysics Domain" (AHEAD-2020), grant No. 871158. S.H. acknowledges support from the Science and Technologies Facilities Council (STFC) through the studentship grant No. ST/V506643/1. Based on observations obtained with XMM-Newton, an ESA science mission with instruments and contributions directly funded by ESA Member States and NASA, and from the NuSTAR mission, a project led by the California Institute of Technology, managed by the Jet Propulsion Laboratory and funded by NASA.

ORCID iDs

V. Braito https://orcid.org/0000-0002-2629-4989
A. Luminari https://orcid.org/0000-0002-1035-8618
D. Porquet https://orcid.org/0000-0001-9731-0352
G. Matzeu https://orcid.org/0000-0003-1994-5322
S. Hagen https://orcid.org/0000-0002-5075-7920

References

Bianchi, S., Guainazzi, M., Matt, G., et al. 2007, A&A, 467, L19
Boroson, T. A. 2002, ApJ, 565, 78
Braito, V., Reeves, J. N., Matzeu, G., et al. 2022, ApJ, 926, 219
Braito, V., Reeves, J. N., Severgnini, P., et al. 2021, MNRAS, 500, 291
Burrows, D. N., Hill, J. E., Nousek, J. A., et al. 2005, SSRv, 120, 165
Chartas, G., Brandt, W. N., Gallagher, S. C., & Garmire, G. P. 2002, ApJ, 579, 169
Chartas, G., & Canas, M. H. 2018, ApJ, 867, 103
Chartas, G., Cappi, M., Vignali, C., et al. 2021, ApJ, 920, 24
den Herder, J. W., Brinkman, A. C., Kahn, S. M., et al. 2001, A&A, 365, L7
Di Matteo, T., Springel, V., & Hernquist, L. 2005, Natur, 433, 604
Fabian, A. C. 1999, MNRAS, 308, L39
Faucher-Giguère, C.-A., & Quataert, E. 2012, MNRAS, 425, 605
Fukumura, K., Dadina, M., Matzeu, G., et al. 2022, ApJ, 940, 6
Fukumura, K., Kazanas, D., Contopoulos, I., et al. 2010, ApJL, 723, L228
Fukumura, K., Kazanas, D., Shrader, C., et al. 2018, ApJL, 864, L27
Giustini, M., & Proga, D. 2019, A&A, 630, A94
Giustini, M., Rodríguez Hidalgo, P., Reeves, J. N., et al. 2023, A&A, 679, A73
Gofford, J., Reeves, J. N., McLaughlin, D. E., et al. 2015, MNRAS, 451, 4169
Gofford, J., Reeves, J. N., Tombesi, F., et al. 2013, MNRAS, 430, 60
Grupe, D., Wills, B. J., Leighly, K. M., et al. 2004, AJ, 127, 156
Hagino, K., Odaka, H., Done, C., et al. 2016, MNRAS, 461, 3954
Harrison, F. A., Craig, W. W., Christensen, F. E., et al. 2013, ApJ, 770, 103
Hopkins, P. F., & Elvis, M. 2010, MNRAS, 401, 7
Hu, C., Li, S.-S., Yang, S., et al. 2021, ApJS, 253, 20
Igo, Z., Parker, M. L., Matzeu, G. A., et al. 2020, MNRAS, 493, 1088
Iwasawa, K., & Taniguchi, Y. 1993, ApJL, 413, L15
Jansen, F., Lumb, D., Altieri, B., et al. 2001, A&A, 365, L1

Jiang, J., Walton, D. J., Parker, M. L., et al. 2018, MNRAS, 481, 639
Kalberla, P. M. W., Burton, W. B., Hartmann, D., et al. 2005, A&A, 440, 775
Kallman, T. R., Palmeri, P., Bautista, M. A., Mendoza, C., & Krolik, J. H. 2004, ApJS, 155, 675
King, A. R. 2003, ApJ, 596, L27
King, A. R., & Pounds, K. A. 2003, MNRAS, 345, 657
Kosec, P., Buisson, D. J. K., Parker, M. L., et al. 2018, MNRAS, 481, 947
Kosec, P., Zoghbi, A., Walton, D. J., et al. 2020, MNRAS, 495, 4769
Lanzuisi, G., Matzeu, G., Baldini, P., et al. 2024, A&A, in press
Laurenti, M., Luminari, A., Tombesi, F., et al. 2021, A&A, 645, A118
Longinotti, A. L., Krongold, Y., Guainazzi, M., et al. 2015, ApJL, 813, L39
Luminari, A., Marinucci, A., Bianchi, S., et al. 2023, ApJ, 950, 160
Luminari, A., Nicastro, F., Elvis, M., et al. 2021, A&A, 646, A111
Luminari, A., Piconcelli, E., Tombesi, F., et al. 2018, A&A, 619, A149
Luminari, A., Piconcelli, E., Tombesi, F., et al. 2024, A&A, submitted
Luminari, A., Tombesi, F., Piconcelli, E., et al. 2020, A&A, 633, A55
Matzeu, G. A., Brusa, M., Lanzuisi, G., et al. 2023, A&A, 670, A182
Matzeu, G. A., Lieu, M., Costa, M. T., et al. 2022, MNRAS, 515, 6172
Matzeu, G. A., Reeves, J. N., Braito, V., et al. 2017, MNRAS, 472, L15
Middei, R., Nardini, E., Matzeu, G. A., et al. 2023, A&A, 680, A50
Mizumoto, M., Nomura, M., Done, C., et al. 2021, MNRAS, 503, 1442
Nardini, E., Reeves, J. N., Gofford, J., et al. 2015, Sci, 347, 860
Nomura, M., Ohsuga, K., & Done, C. 2020, MNRAS, 494, 3616
Osterbrock, D. E., & Pogge, R. W. 1985, ApJ, 297, 166
Parker, M. L., Alston, W. N., Buisson, D. J. K., et al. 2017, MNRAS, 469, 1553
Parker, M. L., Matzeu, G. A., Matthews, J. H., et al. 2022, MNRAS, 513, 551
Pinto, C., Alston, W., Parker, M. L., et al. 2018, MNRAS, 476, 1021
Pounds, K. A., Reeves, J. N., King, A. R., et al. 2003, MNRAS, 345, 705
Pounds, K. A., & Vaughan, S. 2012, MNRAS, 423, 165
Proga, D., & Kallman, T. R. 2004, ApJ, 616, 688
Rakshit, S., Stalin, C. S., & Kotilainen, J. 2020, ApJS, 249, 17
Reeves, J. N., & Braito, V. 2019, ApJ, 884, 80
Reeves, J. N., Braito, V., Gofford, J., et al. 2014, ApJ, 780, 45
Reeves, J. N., Braito, V., Nardini, E., et al. 2018, ApJL, 854, L8
Reeves, J. N., Braito, V., Porquet, D., et al. 2023, ApJ, 952, 52
Reeves, J. N., O'Brien, P. T., & Ward, M. J. 2003, ApJL, 593, L65
Saez, C., & Chartas, G. 2011, ApJ, 737, 91
Schmidt, M., & Green, R. F. 1983, ApJ, 269, 352
Silk, J., & Rees, M. J. 1998, A&A, 331, L1
Sim, S. A., Long, K. S., Miller, L., & Turner, T. J. 2008, MNRAS, 388, 611
Sim, S. A., Miller, L., Long, K. S., Turner, T. J., & Reeves, J. N. 2010, MNRAS, 404, 1369
Sim, S. A., Proga, D., Miller, L., Long, K. S., & Turner, T. J. 2010, MNRAS, 408, 1396
Strüder, L., Briel, U., Dennerl, K., et al. 2001, A&A, 365, L18
Takeuchi, S., Ohsuga, K., & Mineshige, S. 2013, PASJ, 65, 88
Tashiro, M., Maejima, H., Toda, K., et al. 2020, Proc. SPIE, 11444, 1144422
Titarchuk, L. 1994, ApJ, 434, 570
Tombesi, F., Cappi, M., Reeves, J. N., et al. 2010, A&A, 521, A57
Tombesi, F., Cappi, M., Reeves, J. N., et al. 2013, MNRAS, 430, 1102
Tombesi, F., Meléndez, M., Veilleux, S., et al. 2015, Natur, 519, 436
Turner, M. J. L., Abbey, A., Arnaud, M., et al. 2001, A&A, 365, L27
Wilms, J., Allen, A., & McCray, R. 2000, ApJ, 542, 914